HAL
open science

Stress and strain patterns, kinematics and deformation mechanisms in a basement-cored anticline: Sheep Mountain Anticline, Wyoming

Khalid Amrouch, Olivier Lacombe, Nicolas Bellahsen, Jean-Marc Daniel, Jean-Paul Callot

To cite this version:

Khalid Amrouch, Olivier Lacombe, Nicolas Bellahsen, Jean-Marc Daniel, Jean-Paul Callot. Stress and strain patterns, kinematics and deformation mechanisms in a basement-cored anticline: Sheep Mountain Anticline, Wyoming. Tectonics, 2010, 29 (1), pp.n/a - n/a. 10.1029/2009TC002525 . hal-00569489

HAL Id: hal-00569489

https://hal.science/hal-00569489v1

Submitted on 24 Nov 2016

HAL is a multi-disciplinary open access archive for the deposit and dissemination of scientific research documents, whether they are published or not. The documents may come from teaching and research institutions in France or abroad, or from public or private research centers.

L'archive ouverte pluridisciplinaire **HAL**, est destinée au dépôt et à la diffusion de documents scientifiques de niveau recherche, publiés ou non, émanant des établissements d'enseignement et de recherche français ou étrangers, des laboratoires publics ou privés.

TECTONICS, VOL. 29, TC1005, doi:10.1029/2009TC002525, 2010

Click Here for Full Article

Stress and strain patterns, kinematics and deformation mechanisms in a basement-cored anticline: Sheep Mountain Anticline, Wyoming

Khalid Amrouch,[1,2] Olivier Lacombe,[1] Nicolas Bellahsen,[1] Jean-Marc Daniel,[2] and Jean-Paul Callot[2]

Received 6 May 2009; revised 4 September 2009; accepted 22 September 2009; published 27 February 2010.

[1] In order to characterize and compare the stress-strain record prior to, during, and just after folding at the macroscopic and the microscopic scales and to provide insights into stress levels sustained by folded rocks, we investigate the relationship between the stress-strain distribution in folded strata derived from fractures, striated microfaults, and calcite twins and the development of the Laramide, basement-cored Sheep Mountain Anticline, Wyoming. Tectonic data were mainly collected in Lower Carboniferous to Permian carbonates and sandstones. In both rock matrix and veins, calcite twins recorded three different tectonic stages: the first stage is a pre-Laramide (Sevier) layer-parallel shortening (LPS) parallel to fold axis, the second one is a Laramide LPS perpendicular to the fold axis, and the third stage corresponds to Laramide late fold tightening with compression also perpendicular to the fold axis. Stress and strain orientations and regimes at the microscale agree with the polyphase stress evolution revealed by populations of fractures and striated microfaults, testifying for the homogeneity of stress record at different scales through time. Calcite twin analysis additionally reveals significant variations of differential stress magnitudes between fold limbs. Our results especially point to an increase of differential stress magnitudes related to Laramide LPS from the backlimb to the forelimb of the fold possibly in relation with motion of an underlying basement thrust fault that likely induced stress concentrations at its upper tip. This result is confirmed by a simple numerical model. Beyond regional implications, this study highlights the potential of calcite twin analyses to yield a representative quantitative picture of stress and strain patterns related to folding. **Citation:** Amrouch, K., O. Lacombe, N. Bellahsen, J.-M. Daniel, and J.-P. Callot (2010), Stress and strain patterns, kinematics and deformation mechanisms in a basement-cored anticline: Sheep Mountain Anticline, Wyoming, *Tectonics*, *29*, TC1005, doi:10.1029/2009TC002525.

[1]ISTEP, UMR 7193, Université Pierre et Marie Curie, CNRS, Paris, France.

[2]Division Géologie-Géochimie-Géophysique, Institut Français du Pétrole, Rueil-Malmaison, France.

Copyright 2010 by the American Geophysical Union.
0278-7407/10/2009TC002525$12.00

1. Introduction and Aim of the Study

[2] Folding in sedimentary rocks results from two major mechanisms: buckling due to lateral tectonic compression and slip on thrust faults in the underlying strata [e.g., *De Sitter*, 1956; *Faill*, 1973; *Ramsay*, 1974; *Dahlstrom*, 1990]. The overall kinematics may include significant rigid body translations and rotations (e.g., flexural slip) [*Price and Cosgrove*, 1990], as well as considerable straining and/or fracturing of folded strata [e.g., *Sanz et al.*, 2007].

[3] Fractures are the most common macroscopic response of strata to folding [e.g., *Engelder*, 1987; *Engelder et al.*, 1997]. The analysis of the spatial distribution of orientations and densities of fractures between the different fold sectors and their correlation with geometrical attributes such as dip and curvature are commonly used to discuss the relationship between the development of the structural fabric and folding [e.g., *Stearns*, 1968; *Stearns and Friedman*, 1972; *Hennings et al.*, 2000; *Silliphant et al.*, 2002; *Bergbauer and Pollard*, 2004; *Tavani et al.*, 2006; *Bellahsen et al.*, 2006a; *Ahmadhadi et al.*, 2008].

[4] In contrast, description of internal deformation of folded strata and characterization of controlling mechanisms at the microscopic scale have received less attention, so the mechanical response of rocks during folding and the distribution of strain within the fold remain poorly understood. Three different deformation stages have been recognized during fold development. A prefolding phase of diffuse deformation is expressed by layer-parallel shortening (LPS), a folding phase during which the deformation is localized at the hinge and/or is accommodated by flexural slip in the limbs and a late stage fold tightening phase. During these phases, the relative contributions of fracturing and matrix deformation in the accommodation of internal strain of strata are largely unknown. The mechanisms active during the LPS stage for sandstone lithologies have been partly elucidated [*Frizon de Lamotte et al.*, 2002; *Saint-Bezar et al.*, 2002; *Sans et al.*, 2003; *Robion et al.*, 2007]. On the contrary, it is only recently that some studies have been able to quantitatively characterize some mechanisms operating during carbonate rock deformation and to describe the evolution of the associated microstructures [*Evans et al.*,

2003; *Marfil et al.*, 2005; *Evans and Elmore*, 2006; *Graham*, 2006].

[5] Moreover, as emphasized by *Sanz et al.* [2008], stresses that develop during folding likely show a complex pattern and evolution in space and time since they are potentially affected by the interaction between deforming rock layers with different mechanical properties [e.g., *McConaughy and Engelder*, 2001; *Bourne*, 2003], the interfacial condition of the layer boundaries and the presence or absence of bed-parallel slip [e.g., *Couples and Lewis*, 2000; *Johnson and Johnson*, 2000; *Cooke and Underwood*, 2001; *Guiton et al.*, 2003a, 2003b]. The stress distribution is expected to change over time due to fold amplification, bedding rotation [*Fischer and Wilkerson*, 2000; *Engelder and Peacock*, 2001], and reactivation of early formed fractures [e.g., *Wilkins et al.*, 2001; *Bellahsen et al.*, 2006a; *Fiore*, 2006]. Slip along an underlying fault can additionally locally perturb the surrounding stress field, inhibiting development of LPS-related fractures above the fault before fold growth [*Bellahsen et al.*, 2006b]. Some efforts have been devoted to constrain stress evolution in folds using numerical modeling and to compare the results to types and distribution of natural fractures [e.g., *Guiton et al.*, 2003a, 2003b; *Sanz et al.*, 2008]. However, there are only few attempts at characterizing stress patterns in both orientations and magnitudes at the microscopic scale in a fold. So to date, the appraisal of the mechanical behavior of folded strata remains mainly based on observations of macroscopic fracture patterns and comparison with numerical modeling.

[6] In order to characterize and compare the stress record at the macroscopic and the microscopic scales, and to provide direct insights into stress levels sustained by rocks during folding, we investigate the relationship between fold development and stress-strain distribution in strata derived from fractures, striated microfaults and calcite twins. Understanding of the kinematics and structural evolution of folds has greatly benefited from the analyses of such stress-strain indicators, but only a few studies have attempted to define both stress orientations and magnitudes related to folding [*Lacombe et al.*, 1996a; *Lacombe*, 2001]. The main goal of this study is to characterize stress and strain patterns (both orientations and magnitudes) and the relationships between macroscopic and microscopic deformation in a well-exposed fold. To achieve this objective, we rely upon a combination of various techniques: inversion of fault slip data, analysis of fracture sets and analysis of calcite twin data. For the latter, we used both calcite stress inversion and strain gauge techniques that were never used together and even never previously compared.

[7] The basement-cored Sheep Mountain Anticline (SMA) (Wyoming) is taken hereinafter as a case study. This Laramide fold offers the double opportunity to study sedimentary strata in a well-exposed fold and to investigate the influence of an underlying basement thrust fault. Stress and strain patterns all over the SMA are deciphered by carrying out analyses of calcite twins, fractures and striated faults within the various outcropping formations. Special attention is paid to the timing of the calcite twinning and faulting relative to fold development. The results are compared to already available and newly collected mesoscale fracture data. Prefolding and postfolding stress and strain orientations and magnitudes are investigated in both the forelimb and the backlimb, thus providing for the first time an integrated picture of stress distribution during folding above a basement thrust fault. This study finally helps to constrain the mechanical behavior of folded strata and the deformation mechanisms active at different scales during folding.

2. Geological Setting

2.1. Laramide Uplifts ("Arches")

[8] The Rocky Mountain uplifts consist of isolated basement highs and folds in the foreland of the Sevier thrust belt, associated to high-angle thrust faults rooted deep in the basement [*Stone*, 1993; *Erslev*, 1993] (Figure 1). Among them, the Bighorn Mountains in Wyoming consist of an elongate, NW trending foreland uplift separating the Bighorn basin to the west from the Powder River basin to the east.

[9] Stratigraphic study of basins flanking these uplifts [*Dickinson et al.*, 1988] demonstrate that all the uplifts and related thrusts were initiated simultaneously during the Maastrichtian, during the Laramide orogeny. *Marshak et al.* [2000] suggest that the high-angle thrusts responsible for basement uplifts may result from the inversion of Proterozoic extensional faults. Alternatively, Sheep Mountain and other similar anticlines in the Bighorn basin have a distinct thinning of the Pennsylvanian Tensleep formation over their crests, which suggest that they are sited over previous highs which probably formed over Paleozoic faults active during the Ancestral Rocky Mountain Orogeny (E. A. Erslev, personal communication, 2009).

[10] Among the Laramide uplifts, the Sheep Mountain Anticline (SMA) is an asymmetric basement-cored fold [*Erslev*, 1993] located along the western edge of the Bighorn basin (Figure 1). The fold trends NW-SE and is NE verging. The Bighorn River cuts the anticline normal to the fold axis, thus providing a complete section of the cover.

2.2. Stratigraphy of the Bighorn Basin

[11] The Bighorn Basin was filled by 3000 m of sediments during the Paleozoic and Mesozoic [*Thomas*, 1965; *Ladd*, 1979, *Hennier and Spang*, 1983; *Rioux*, 1994; *Forster et al.*, 1996].

[12] The Cambrian (Flathead, Gros Ventre, and Gallatin formations), Ordovician (Big Horn Formation), and Devonian (Jefferson–Three Forks formations) sequences consist of about 500 m of shales, limestones, and dolomites which are not exposed at SMA.

[13] Four formations crop out at SMA (Figure 2). The oldest exposed formation is the Lower Mississippian Madison limestones (230 m thick) [*Sonnenfeld*, 1996]. This unit is overlain by the Carboniferous Amsden Formation (35 m thick), mainly composed of cross-bedded, light gray fine-grained quartz arenites [*Ladd*, 1979]. The Upper

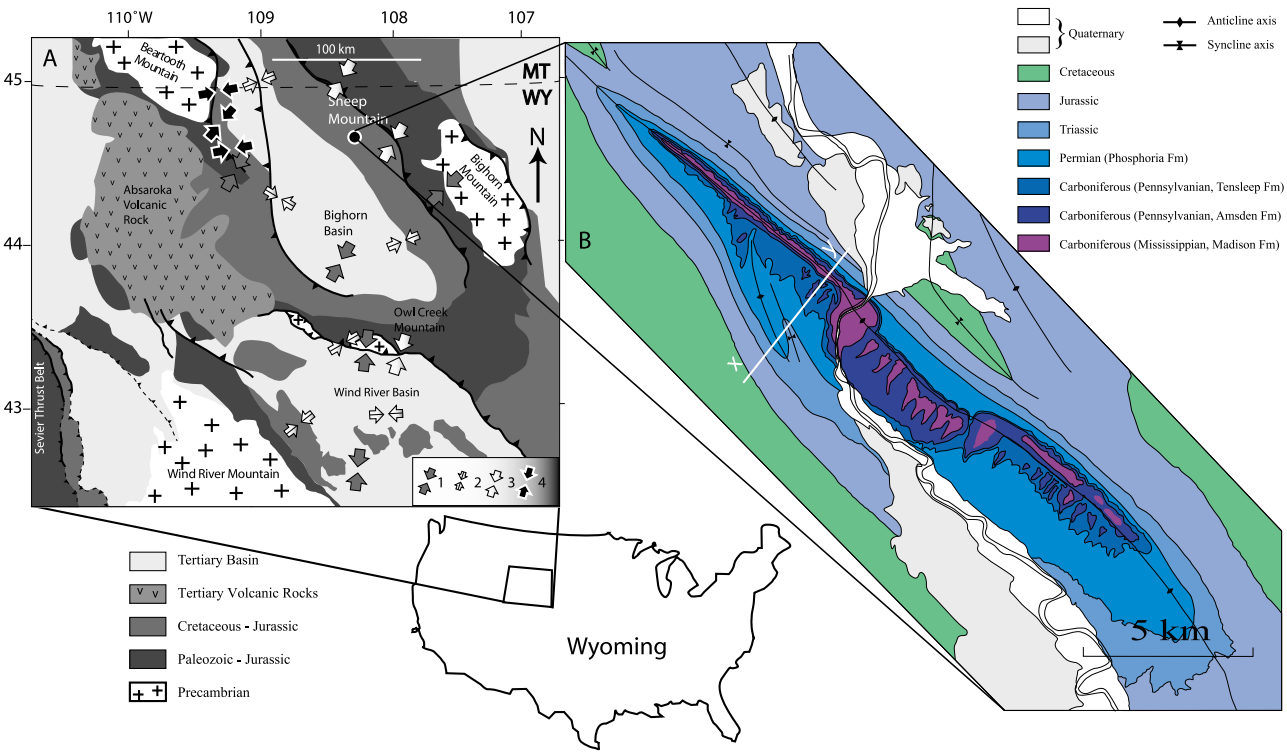

Figure 1. (a) Simplified geological map of Laramide uplifts in Wyoming. Arrows indicate Laramide and Sevier compression trends reconstructed by different authors: 1, Laramide compressional trend from *Craddock and van der Pluijm* [1999]; 2, Sevier compressional trend from *Craddock and van der Pluijm* [1999]; 3, Laramide compressional trend from *Varga* [1993]; 4, Laramide compressional trend from *Neely and Erslev* [2009]. (b) Geological map of Sheep Mountain Anticline. X-Y, location of cross section of Figure 3.

Pennsylvanian Tensleep Formation (29 m thick) is composed of interbedded thin sandstones, shales, and carbonates in its lower part and thicker beds of cross-bedded quartz arenites in its upper part. The Permian is represented by the 70 m of the Phosphoria Formation: predominantly siltstones and shales with a thin interbedded gypsum layer overlain by thick carbonates [*Ladd*, 1979]. The Phosphoria Formation is topped by the argilaceous Chugwater Formation of Triassic age. The overlying Mesozoic sediments are composed of sandstones, shales, and few carbonates that are preserved in synclines surrounding SMA (Figure 2).

2.3. Geometry of Sheep Mountain Anticline

[14] Sheep Mountain Anticline is a basement-cored, doubly plunging, asymmetric fold (Figures 1 and 3). Its NW–SE trend (Figure 1) is similar to that of many folds within the Rocky Mountains, although some others formed at acute angles to the regional compression [*Erslev*, 1993]. This fold formed during the Laramide orogeny under a NE trending compression at the end of the Maastrichtian and during Paleocene times [*Dickinson and Snyder*, 1978; *Engebretson et al.*, 1985; *Bird*, 1998, 2002].

[15] The steep northeastern limb (forelimb) of SMA dips between 40° and 90° northeast. This dip is shallower near the fold pericline and steeper in the central part of the fold. In the southwestern limb (backlimb), bedding dips are between 10° and 40° southwest. Near the northern termination, the fold axe plunges approximately 20° northwest and the fold is quite tight, while toward the south, the asymmetry increases and the curvature at the hinge decreases. At the southern termination, the plunge of the fold axis is approximately 10° southeast.

[16] At depth, the structure of the fold remains largely unconstrained. The fold overlies a fault that has been interpreted as a SW dipping thrust [*Hennier and Spang*, 1983; *Erslev*, 1993; *Forster et al.*, 1996; *Stanton and Erslev*, 2004]. *Stanton and Erslev* [2004] suggested that this thrust was later cut by a NE dipping thrust below the southern syncline. This fault chronology disagrees with that of *Hennier and Spang* [1983] and *Forster et al.* [1996], who argued that the SMA fault is a SW dipping back thrust of an older NE dipping thrust. *Stone* [2004] proposed that the SW and NE dipping thrusts developed contemporaneously in Laramide times.

[17] In the back limb, a smaller fold ("thumb") branches on the main anticline, trending NNW–SSE. Because of its wavelength, this structure was interpreted as a "rabbit ear" related to a shallower thrust fault with no implication of the basement [*Hennier and Spang*, 1983; *Forster et al.*, 1996; *Savage and Cooke*, 2004; *Stanton and Erslev*, 2004].

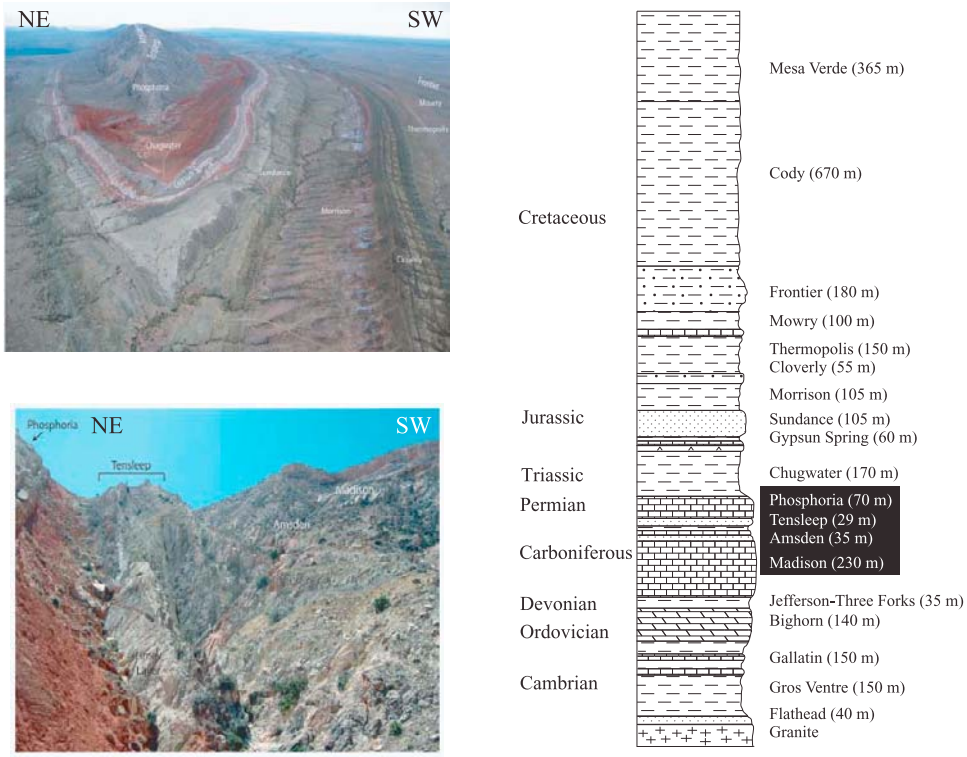

Figure 2. Stratigraphic section [after *Ladd*, 1979] and pictures of formations that crop out at SMA.

[18] The partially renewed interpretation of the deep structure at SMA shown in Figure 3 does not involve any new sequence of basement faulting, but tries to be consistent with structural features commonly recognized in inversion tectonics such as short cuts and triangle zones that are likely to be encountered at depth [e.g., *Roure et al.*, 1990; *Roure and Colletta*, 1996]. For instance, we favor the reactivation of the underlying SW dipping (normal) fault as

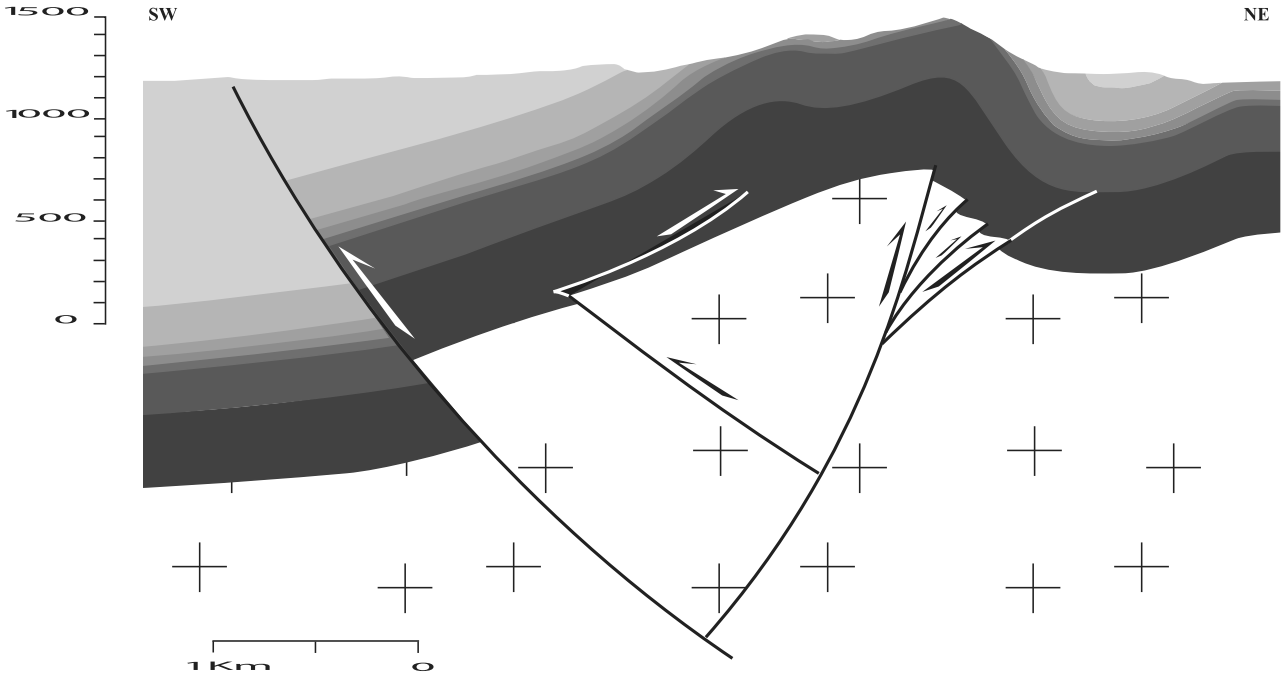

Figure 3. Cross section through SMA (location along X-Y in Figure 1b) modified after *Hennier and Spang* [1983] and *Stanton and Erslev* [2004].

a high-angle thrust fault with a short cut accommodated by many splays in order to account for the relatively distributed deformation required for basement folding. In addition, the small "rabbit ear" (thumb) fold has a trend similar to that of many other basement-cored fold in the Rockies, so that this trend is likely controlled by a basement structure. We therefore propose that the SW dipping shallower thrust below the thumb that roots in a decollement in the clayish Gros Ventre Formation does not merge directly from the master SW verging thrust below the Bighorn basin as suggested by *Stanton and Erslev* [2004] but is rather associated to a triangle zone above a second-order NE dipping basement (normal) fault also reactivated as a high-angle thrust (Figure 3).

[19] As a result, shortening in SMA is accommodated in the sedimentary layers primarily by both folding and internal deformation, whereas it is accommodated in the basement by inversion of preexisting (normal) faults resulting in high-angle thrusts and short cuts. In spite of these differences in deformation style between cover and basement, the value of the shortening is rather similar between the cover and the basement, i.e., ~350 and 500 m, respectively; these values correspond to shortening of approximately ~5% and 7%.

2.4. Sevier Versus Laramide Stresses and the Laramide Uplifts

[20] Previous works have reported a main NE to ENE compressional trend or transport direction related to the Laramide orogeny in the investigated area (Figure 1) [*Hoppin*, 1970; *Sales*, 1968; *Reches*, 1978; *Dickinson and Snyder*, 1978; *Engebretson et al.*, 1985; *Brown*, 1988; *Wise and Obi*, 1992; *Varga*, 1993; *Bird*, 2002]. *Craddock and van der Pluijm* [1999] recently performed a study of Sevier and Laramide strain orientations by the measurement of mechanically twinned calcite from Paleozoic–Mesozoic carbonates. The overall direction of regional LPS fabrics preserved in the carbonates of the Idaho–Wyoming portion of the thrust belt is oriented ENE–WSW, i.e., generally parallel to the Sevier thrust transport direction (~E–W) (Figure 1a). In contrast, synorogenic calcite cements and veins preserve a distinct twinning deformation history: in Laramide uplifts and adjacent basins as far east as the Black Hills, twinned vein calcite preserves a subhorizontal, N–S shortening strain, regardless of the vein orientation. These authors concluded that deformation of the plate interior during the Sevier orogeny was dominated by E–W contraction at the plate margin, which changed into dominantly oblique contraction (N–S shortening) along western North America during the younger, basement-involved Laramide event.

[21] Reported stress orientations near frontal fault zones of Laramide age foreland uplifts in Wyoming [*Varga*, 1993, Figure 1] are compatible with horizontal compression at high angles to the frontal fault zones and to the general trends of the uplifts. The orientations of the compression directions vary with uplift trend, from nearly E–W (eastern Laramie Range), to NE (Bighorn Mountains) and to N–S (Owl Creek Mountains and Casper Mountains).

[22] Temporal variations in Laramide stress orientations have been proposed [*Chapin and Cather*, 1981, 1983; *Gries*, 1983, 1990; *Bergerat et al.*, 1992). *Chapin and Cather* [1981, 1983] suggested a change in Laramide compression direction from N70°E to N45°E at 55 Ma, whereas *Gries* [1983, 1990] suggested a three-stage rotation of horizontal compression during the Laramide, from approximately E–W (Campanian to Paleocene) to NE–SW (Paleocene) to N–S (Eocene). These authors relate the counterclockwise rotation in principal horizontal stress to changes in the North American plate velocity vector during the opening of the Atlantic. *Gries* [1983, 1990] specifically related variation in orientation of Rocky Mountain foreland uplifts to the suggested temporal changes in compression direction. Other authors rather suggested that the various foreland uplifts in Wyoming formed during a single period of ENE directed [*Sales*, 1968; *Stone*, 1969] or NE directed [*Brown*, 1981, 1988; *Paylor et al.*, 1989; *Blackstone*, 1990] compression. *Varga* [1993] concluded that the dominant Laramide trend was NE and that regionally local deviations may arise from strain partitioning with zones of dominantly compressional deformation and zones of dominantly strike–slip faulting along E–W trending structures oblique to the overall Laramide compression.

2.5. Previous Fracture Studies at Sheep Mountain Anticline

[23] The main steps of fracture development in relation to SMA development have been described by *Bellahsen et al.* [2006a] and *Fiore* [2006]. Four fracture sets (sets I to IV) were identified in SMA based on orientation data and deformation mode. Reported fracture orientations for sets I, II, and III are coaxial with bedding and unfolded. Reported orientations for set IV are present-day orientation.

[24] Set I fractures that strike 110°, oblique to the fold trend, are interpreted as a regional fracture set that was present before the Laramide anticline and originated in a different stress field. Set II joints striking 045° and observed in the hinge and the backlimb, are interpreted as related to the NE oriented Laramide compression just prior to and during initial anticline growth (LPS joints). Joints striking 135° (set III), nearly parallel to the fold trend, are found mainly in the hinge and are interpreted to have formed in response to bending stresses during folding. Set IV corresponds to vertical joints oblique to the fold axis and striking 110° that may have developed in the backlimb in response to stress relaxation during fold exhumation. *Bellahsen et al.* [2006a, 2006b] inferred that the fracture pattern suggests a fixed hinge folding mode with little lateral propagation of the underlying SW dipping thrust fault and of the anticline, and that the forelimb was located in the early stage of folding of SMA in the hanging wall of the basement thrust fault.

3. Methods for Characterizing Stress and Strain Patterns in SMA

[25] In order to investigate the stress record during folding at both macroscopic and microscopic scales, we

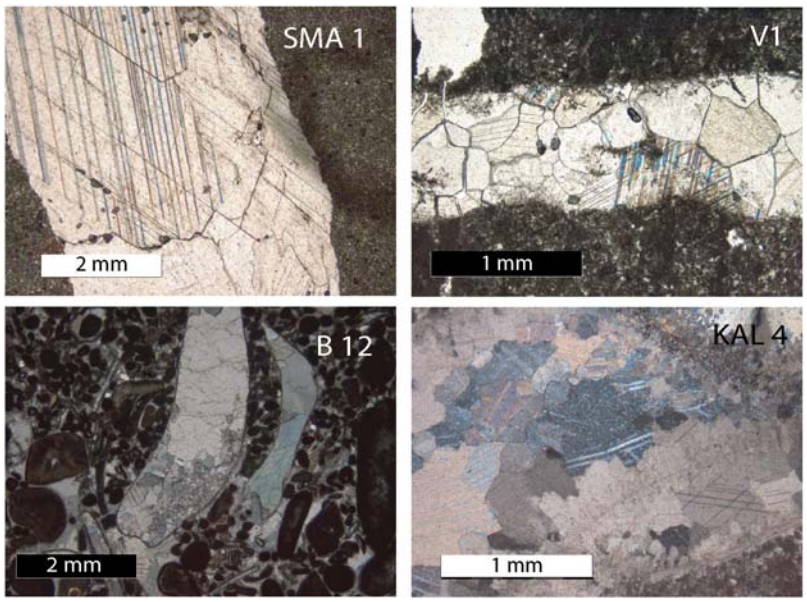

Figure 4. Photographs of twinned grains from veins and matrix from studied samples. Vein SMA1 belongs to set I, while V1 vein belongs to set II. SMA 1, Madison Formation; V1, Phosphoria Formation; B 12, Thermopolis Formation; Kal 4, Madison Formation.

carried out a study of striated microfaults and calcite twins. Combination of both methodologies has proven to be an efficient tool to characterize paleostress fields in terms of both stress orientations and magnitudes during development of fold-thrust belts as well as of individual fold structures [e.g., *Lacombe et al.*, 1993, 1996a, 1996b, 2007; *Lacombe*, 2001]. The results are compared to the results of a new study of fracture sets in SMA.

3.1. Calcite Twins Analysis

[26] Widespread mechanical e-twinning occurs in calcite deformed at low temperature (Figure 4). The e-twinning requires a low critical resolved shear stress (RSS) (10 ± 4 MPa), which depends on grain size [e.g., *Rowe and Rutter*, 1990] and internal twinning strain [*Turner et al.*, 1954; *Laurent et al.*, 2000; *Lacombe*, 2001, 2007], and has only a small sensitivity to temperature, strain rate and confining pressure. Twinning is possible along three glide $\{01\bar{1}2\}$ planes. Depending on the orientation of the principal stresses, twinning may occur on any or all of these twin planes.

[27] Several methods for determining stress or strain components from calcite twin lamellae have already been proposed (see review by *Burkhard* [1993]). For this study, we used Etchecopar's calcite stress inversion technique (CSIT) [*Etchecopar*, 1984] (see details in work by *Lacombe* [2001, 2007]) to obtain the stress tensor, while Groshong's calcite strain gauge technique (CSGT) [*Groshong*, 1972] allows production of a strain ellipsoid. The CSIT applies to small twinning strain that can be approximated by coaxial conditions, so orientation of twinning strain can be correlated with paleostress orientation.

3.1.1. Determination of the Paleodeviatoric Stress

[28] The inversion process takes into account both the twinned and the untwinned planes, the latter being those of the potential e-twinning planes that never experienced a RSS of sufficient magnitude to cause twinning. The inverse problem consists in finding the stress tensor that best fits the distribution of twinned and untwinned planes. The basic hypothesis is that the RSS τ_s acting on any twinned e plane is higher than, or at least equal to the critical RSS τ_a. Thus, for twinned planes: $\tau_s \geq \tau_a$ and for untwinned planes: $\tau_s < \tau_a$.

[29] Etchecopar's CSIT allows simultaneous computation of principal stress orientations and differential stresses. The tensor solution is calculated as a normalized reduced stress tensor such as $(\sigma_1 - \sigma_3)$ is scaled to 1 $[(\sigma_1 - \sigma_3)^* = 1]$. Thus, the value of the RSS τ_s acting on any plane lies between -0.5 and $+0.5$, that is, $-(\sigma_1 - \sigma_3)^*/2$ and $+(\sigma_1 - \sigma_3)^*/2$ [*Jamison and Spang*, 1976]. Theoretically, all the twinned planes consistent with a given tensor must sustain a τ_s value larger than the one exerted on any untwinned plane. The best tensor solution is searched as to minimize the function f, ideally equal to 0, defined as

$$f = \sum_{j=1}^{N} \left(\tau_{sj} - \tau_{a'}\right),$$

where $\tau_{a'}$ is the smallest RSS applied on the twinned planes compatible with the tensor and τ_{sj} are the RSS applied on the N untwinned planes j such that $\tau_{sj} > \tau_{a'}$ (for more details, see *Etchecopar* [1984] and *Laurent* [1984]). The $\tau_{a'}$ value is deduced from the inversion and corresponds to the critical RSS for the normalized tensor used for calculation.

[30] The optimal tensor is obtained when (1) the maximum of twinned planes are taken into account; (2) the maximum of untwinned planes are taken into account; and (3) the f value is minimal (in practice, one can authorize a weak percentage, 10%–15%, of untwinned planes receiving a RSS larger than $\tau_{a'}$ because of measurement uncertainties and local heterogeneities at the grain scale).

[31] This process leads to the determination of the orientations of the principal stresses σ_1, σ_2, and σ_3 and the stress ellipsoid shape ratio, $\phi = (\sigma_2 - \sigma_3)/(\sigma_1 - \sigma_3)$ with $0 \leq \phi \leq 1$.

[32] The access to the fifth parameter of the tensor is possible because of the existence of a constant critical RSS τ_a:

$$(\sigma_1 - \sigma_3) = \frac{\tau a}{\tau a'} x (\sigma_1 - \sigma_3)^* = \frac{\tau a}{\tau a'}$$

The final result is the determination of the five parameters of the deviatoric tensor responsible for the twinning: the σ_1, σ_2 and σ_3 orientations, and the differential stress values $(\sigma_1 - \sigma_3)$ and $(\sigma_2 - \sigma_3)$. Uncertainties on computed stress orientations are about 10°–15°; uncertainties on differential stress values are ±20%; the latter partly arise from sample purity and local facies changes within stratigraphic horizons across the study area [e.g., *van der Pluijm et al.*, 1997] and from the methodology used [e.g., *Lacombe and Laurent*, 1996; *Laurent et al.*, 2000].

[33] When more than ~30% twinned planes in a sample are not explained by a unique stress tensor, the inversion process is repeated with the uncorrelated twinned planes and the whole set of untwinned planes. This procedure provides an efficient way to separate superimposed twinning events and to calculate related stress tensors where polyphase deformation has occurred.

[34] The CSIT is to date the only technique that allows simultaneous calculation of principal stress orientations and differential stress magnitudes from a set of twin data, therefore allowing to relate unambiguously differential stress magnitudes to a given stress orientation and stress regime. Numerous studies have demonstrated its potential to derive regionally significant stress patterns, even in polyphase tectonics settings [e.g., *Lacombe et al.*, 1990, 1993, 1996a; *Rocher et al.*, 1996, 2000, and references therein].

3.1.2. Determination of the Strain Ellipsoid

[35] The CSGT [*Groshong*, 1972, 1974] allows computation of the strain ellipsoid. Strain magnitudes vary greatly, however, depending on factors such as lithology, grain size and porosity, and are a function of twin thickness. The results of *Evans and Dunne* [1991] and *Groshong et al.* [1984] demonstrated that the calcite strain gauge gives quite accurate measurement of the orientations of the principal strain axes up to 17% of strain.

[36] Groshong's CSGT takes into account the widths of thin and thick twins. For each twin set measured, the average twin width, number of twins, grain width normal to twins, and the orientations of the c axis and the e-twin plane are measured. In general, widths of thin and thick twins are measured separately. However, in our samples only thin twins could be observed. The principal strains (ε_{max}, ε_{int}, and ε_{min}; expressed in % changes in length) and their orientations are calculated. The CSGT also computes positive and negative expected values (PEV and NEV, respectively) for all twins in a given thin section. NEV correspond to twin sets with sense of shear inconsistent with the calculated strain tensor. A high percentage of negative expected values (>40%) indicates that a second, noncoaxial twinning event occurred.

[37] The tensor shear strain for a given twin set in the plane defined by the normal to the e twin plane and the glide direction g[e1:r2] (i.e., the intersection between the e twin plane and the r $\{10\bar{1}1\}$ cleavage plane) is given by

$$\Gamma_{eg} = \frac{1}{2} \tan \psi = \frac{0.347}{w} \sum_{i=1}^{n} t_i,$$

where ψ is the angle of shear, w is the thickness of the grain perpendicular to the twin plane, and $\sum_{i=1}^{n} t_i$ is the total width of the twin lamellae in the set.

[38] The data are treated like strain gauge measurements and a least squares solution is used to find the complete calcite twinning strain tensor for the sample. Principal strain magnitudes and directions are then found using standard eigenvector and eigenvalue analysis. This technique has provided valuable results when applied to fold-thrust belts and forelands [e.g., *Harris and van der Pluijm*, 1998; *Craddock and van der Pluijm*, 1999].

3.2. Analysis of Fault Slip Data

[39] The kinematics of a fault population is defined using striations observed on mesoscale fault planes at many sites. The main objective is to define the successive states of stress and their probable significance in relation to local/regional tectonics. Other stress indicators, such as veins and stylolites help to constrain extensional and compressional trends, respectively. The methodology of fault kinematic studies to determine paleostress fields and identify temporal and spatial stress changes has been used in many areas worldwide over the past 30 years [e.g., *Letouzey*, 1986]. To determine the stress fields associated with fold evolution in the investigated area, we have carried out a quantitative inversion of distinct families of fault slip data determined at each individual site, using the method proposed by *Angelier* [1990].

3.2.1. Assumptions and Basic Mechanical Principles

[40] Fault slip inversion assumes that (1) the analyzed body of rock is physically homogeneous and isotropic and if prefractured, is also mechanically isotropic, i.e., the orientation of fault planes is random, (2) the rock behaves as a rheologically linear material [*Twiss and Unruh*, 1998], (3) displacements on the fault planes are small with respect to their lengths and there is no ductile deformation of the material and thus no rotation of fault planes. Moreover, the computation assumes that (4) a tectonic event is characterized by a single homogeneous stress tensor, (5) the slip responsible for the striation occurs on each fault plane in the direction and the sense of the maximum resolved shear

Table 1. Results of Stress Tensor Determination Based on Fault Slip Data[a]

Site	Formation	Trend (Plunge) of the Principal Stress Axes (deg)			Ratio Between Differential Stresses (Φ)	Number of Data	α (deg)
		σ_1	σ_2	σ_3			
X1	Madison	063 (55)	323 (07)	229 (35)	0.36	9	11.4
		226 (04)[b]	135 (21)[b]	327 (68)[b]	0.36	9	11.4
X2	Tensleep	240 (14)	330 (01)	062 (76)	0.45	7	12.7
		060 (04)[b]	329 (03)[b]	274 (86)[b]	0.45	7	12.7
X5	Tensleep	077 (04)[b]	167 (01)[b]	274 (86)[b]	0.4	22	18.3
X6	Cretaceous	038 (03)	308 (01)	193 (87)	0.47	31	6.3
		209 (00)	299 (64)	119 (26)	0.11	15	13.5
X10	Madison	311 (25)	082 (54)	209 (24)	0.75	5	8.2
		320 (20)[b]	127 (70)[b]	031 (02)[b]	0.75	5	8.2
X7	Phosphoria	219 (03)	310 (12)	116 (78)	0.0	8	6.8
X9	Phosphoria	220 (12)	311 (07)	070 (76)	0.1	19	6.0
		033 (04)	126 (38)	298 (52)	0.23	15	8.0
X15	Madison	042 (05)	132 (02)	239 (84)	0.9	9	6.9
		042 (81)	321 (09)	051 (00)	0.67	10	10.9
X11	Madison	285 (76)	133 (12)	042 (06)	0.0	4	2.7
		217 (20)	125 (05)	023 (70)	0.13	4	7.3
X14	Madison	281 (08)[b]	033 (69)[b]	188 (19)[b]	0.24	6	3.5

[a]Ratio Φ is defined in text; α is average angle between actual slip and computed shear stress.
[b]Back-tilted stress axes.

stress (Wallace-Bott principle), and (6) the slip on each of the fault planes is independent of each other.

[41] The basic principle consists of finding the best fit between the observed directions and senses of slip on numerous faults and the theoretical shear stress induced on these planes by the tensor solution of the inverse problem. The results are the local orientation of the three principal stress axes σ_1, σ_2, and σ_3 and the ϕ ratio. The quality of the tensor calculated is given by numerical estimators such as the average angle between the computed shear stresses and the actual striations on fault surfaces (Table 1). Uncertainties in the principal stress directions depend mainly on the geometric distribution of fault slip data; under optimal conditions, the accuracy on the trend and plunge of stress axes is better than 10°.

3.2.2. Establishing a Relative Chronology Between Successive Faulting Events

[42] The identification and separation of successive generations of faults and related stress regimes is based on both mechanical incompatibility between fault slips (individual misfits of fault slips with the computed stress tensors) and relative chronology observations (superimposed striations on fault surfaces, crosscutting relationships between faults, . . .). Particular attention is also paid to horizontal axis rotations of rock masses due to folding. Where tilted bedding is observed as a result of folding, faults may have formed before, during or after folding (Figure 5). Following *Anderson* [1951], we assume that away from major fault zones, one of the three principal stress axes of a tensor is generally vertical. If a conjugate fault set formed before folding and was secondarily tilted with the bedding, the tensor calculated on this set does not display a vertical axis. Instead, one of the stress axes is generally found perpendicular to bedding, whereas the two others lie within the bedding plane. In such a case, the fault system is interpreted after back tilting to its initial position by rotation along the local strike. In contrast, a conjugate fault system with two horizontal and one vertical principal stress axes irrespective of bedding dip is clearly postfolding. A set of conjugate strike-slip fault system (for instance) with an acute bisector σ_1 inclined consistently less than, but in the same direction as bedding dip likely developed during folding. Within a heterogeneous fault population this geometrical reasoning allows separation of data subsets based on their age relative to fold development. In the case of the relatively simple geometry of SMA, this criterion is of primary importance for establishing a relative chronology. The chronology inferred this way may also be confirmed by identification of superimposed striations on reactivated fault surfaces where observable.

3.3. Analysis of Fracture Sets

[43] New fracture data were collected during recent field surveys [*Fiore*, 2006; this study]. Fracture orientations, lengths, spacing, and modes of deformation (opening or shearing) were recorded, as well as abutting relationships. At each measurement site, all fractures were measured in areas typically a few tens of meters on a side. As in the work by *Bellahsen et al.* [2006a], fracture sets are defined based on orientation, deformation mode and relative chronology. Most of these fractures show opening displacement with no observable shear movements. Some show only microscopic opening displacement and can be classified as joints but most are veins characterized by various thickness of cement. Plumose structures, i.e., common and characteristic features of mode I fractures [*Engelder*, 1987; *Pollard and Aydin*, 1988], are sometimes preserved on their surfaces. In some sites, thin sections were cut in order to check the dominant occurrence of mode I joints and veins, therefore allowing to use these fracture sets as reliable indicators of orientations

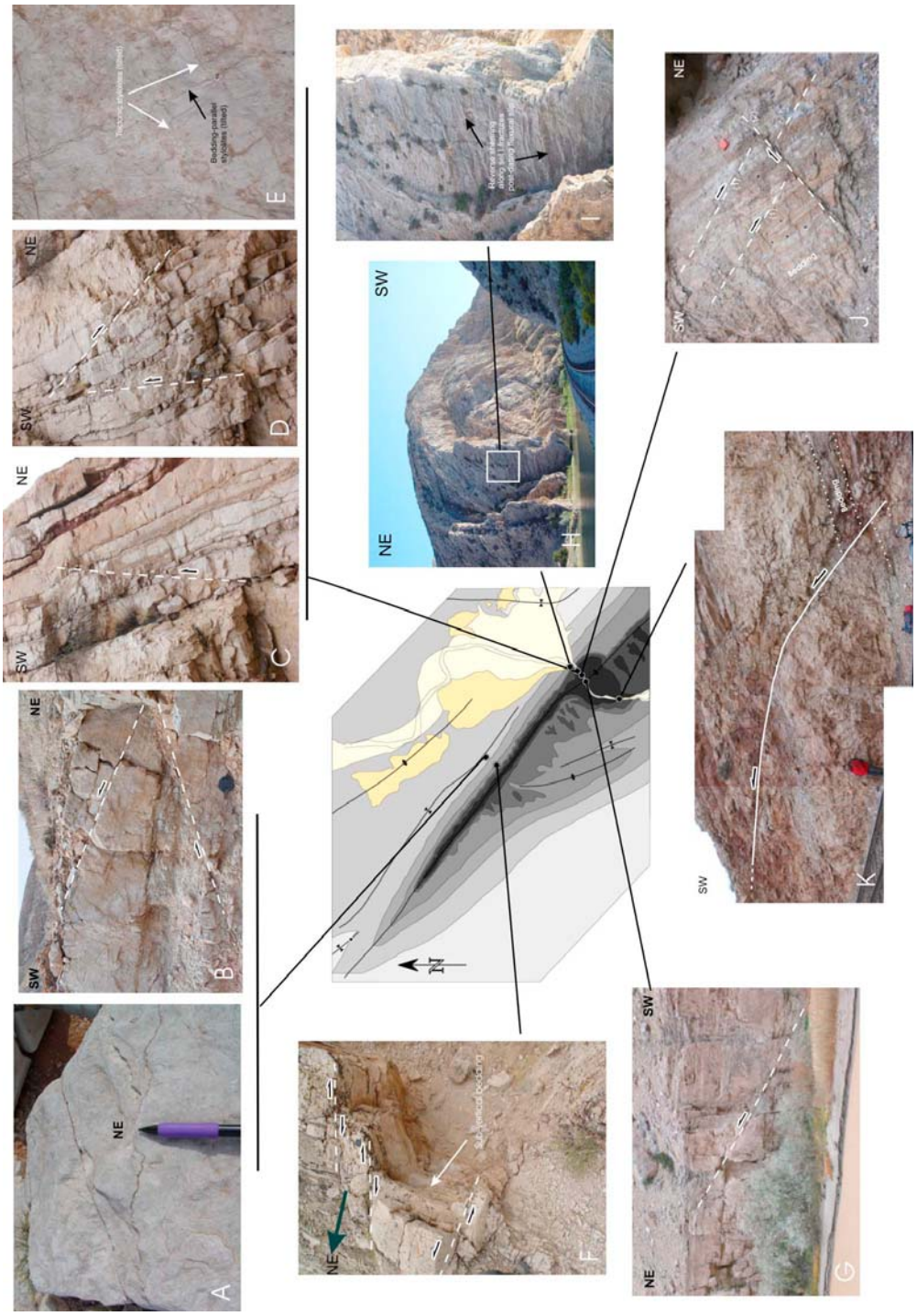

Figure 5. Examples of mesoscale faults and other structures observed in the field. (a) Tectonic stylolites in Cretaceous limestones in the syncline located north of SMA. (b) Conjugate reverse faults in Cretaceous limestones in the syncline located north of SMA. (c and d) Prefolding reverse faults in the forelimb of SMA (Madison Formation). (e) Tectonic and bedding-parallel stylolites in the forelimb of SMA (Madison Formation). (f) Late conjugate strike-slip faults offsetting vertical beds in the forelimb of SMA (Phosphoria). (g) Reverse fault at the hinge of SMA within the canyon (Madison Formation). (h) View of SMA forelimb from the northern end of the canyon of the Bighorn river. (i) Detail of the forelimb beds showing reverse shearing along set I postdating flexural slip (Madison Formation). (j) Example of chronology between reverse faults in the forelimb of SMA (Madison Formation): prefolding reverse faults (1) cut by postfolding reverse fault (2). (k) Example of NE trending reverse fault consistent with NW–SE shortening.

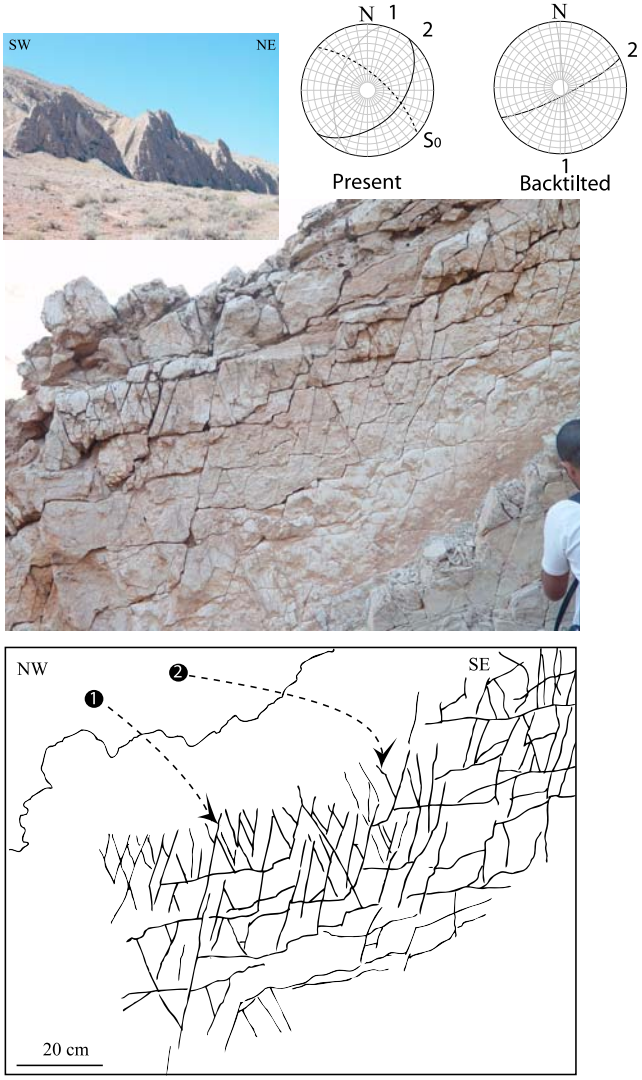

Figure 6a. Detailed views of fractures close to site 11 on steep pavements in the forelimb (Phosphoria Formation). The views are from below the pavement, looking NE.

of paleo-σ_3 trends [*Engelder*, 1987] to be compared with stress directions derived from inversion of fault slip and calcite twin data. In many outcrops, small shear displacements, splay veins (Figures 6a and 6b) and extensional jogs were observed along veins. Such sheared veins were carefully considered to demonstrate further reactivation.

[44] We present hereinafter stereonets of the orientation data (see *Bellahsen et al.* [2006a] for description of the fracture cluster determination code, developed at IFP). The results of this analysis are presented in a polar stereonet using the Lambert projection on the lower hemisphere with great circles representing the mean plane of each fracture set.

3.4. Microstructural Setting and Strategy of Sampling

[45] The Bighorn River cuts through the fold and provides natural exposures of most formations that crop out in SMA. We took advantage of these exceptional exposure conditions to collect rock samples all over the anticline and in all formations, with the aim at investigating the differential mechanical response of the different lithologies (carbonates, sandstones, and shales) affected by the same deformation history. We sampled both matrix and veins, especially prefolding veins (set I) and fold-related veins (sets II and III, Figure 4). Some samples were discarded because the grain size was too small or because they contained gypsum. Fourteen samples were retained for twin analyses.

[46] Sampling both fold limbs constrains the chronology of twinning relative to the folding. As for fault slip data, one might expect that if a twin set formed during the initial phase of LPS and was subsequently tilted with the strata during folding, then one axis of the stress-strain tensor should be perpendicular to bedding and the other two would lie within the bedding plane. In contrast, late or postfolding twin sets should yield two horizontal stress-strain axes and one vertical one (assuming that the regional stress-strain field is in that orientation). The chronology of twinning events and related stress-strain tensors can additionally be constrained by comparing calcite twinning strain preserved in rock matrix (which presumably recorded the entire stress history, or at least the earliest stages since calcite may harden once twinned) and in the different fracture sets (Figure 4).

[47] The coarse grained studied limestones present thin ($\sim$0.5 μm) and rectilinear e-twins, which cross the crystals over all their length (Figure 4). These characteristics indicate that these limestones probably underwent weak strain, 3% to 4% at most, under conditions of temperature lower than 150°C–200°C [*Ferrill et al.*, 2004]. Thirty four independent and representative stress analyses were generated (Table 2), and five samples were independently analyzed to get the strain ellipsoid (Table 3).

4. Results

4.1. Paleostress Orientations and Regimes

4.1.1. Paleostress Orientations From Calcite Twins

[48] Calcite twin analysis reveals three main tectonic stages: two stages of LPS (a prefolding compression nearly parallel to the fold axis and a prefolding compression perpendicular to the fold axis after bedding is restored to horizontal), and a stage of postfolding compression also trending normal to fold axis. Minor extensional stress tensors are also recognized in place. The results are illustrated in Figures 7 to 10; the characteristics of the stress tensors are reported in Table 2.

[49] The first LPS stage (LPS1 hereinafter) corresponds to a N135° directed compression. It is observed in both limbs. LPS1 is preserved by calcite twinning in the matrix of the Madison and Phosphoria formations. All stress tensors correspond to a strike-slip stress regime with nearly horizontal σ_1 and σ_3 axes (Figure 7).

[50] The second LPS stage (LPS2 hereinafter) corresponds to a NE–SW direction of compression with a maximum principal stress axis σ_1 that trends perpendicular

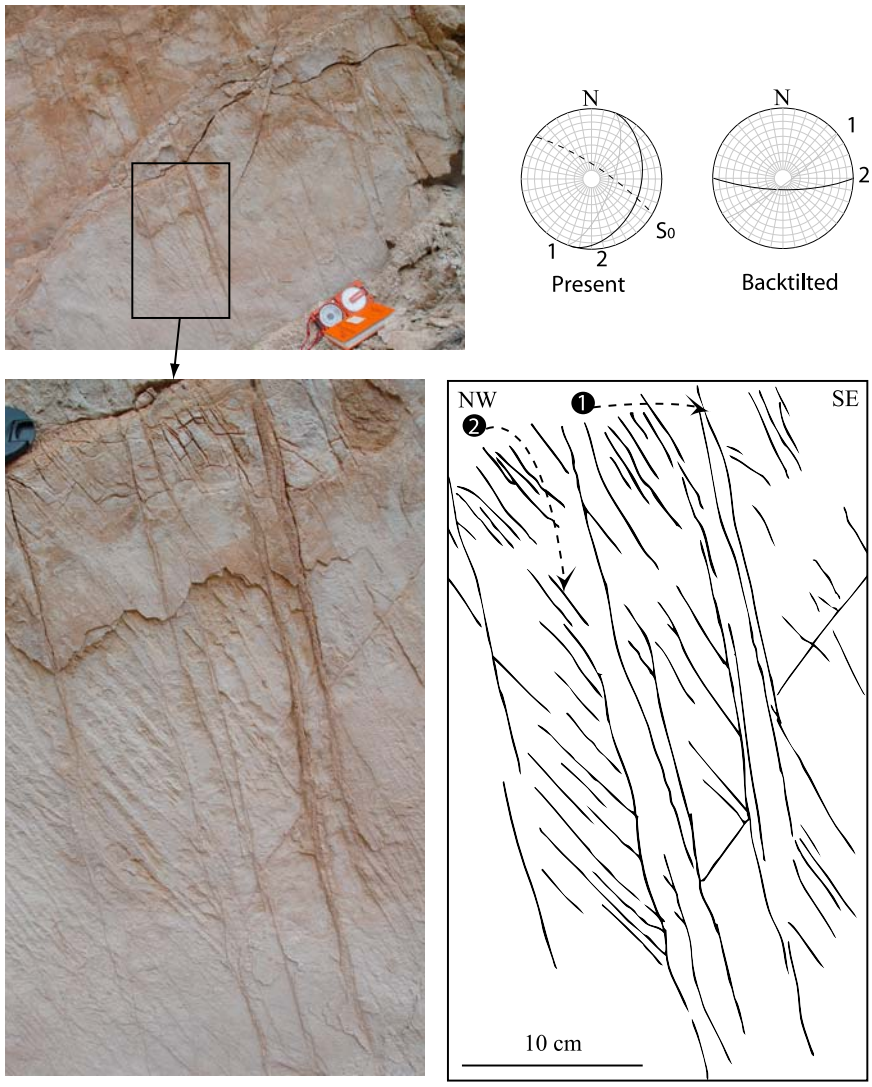

Figure 6b. Detailed views of fractures close to site 12 on steep pavements in the forelimb (Phosphoria Formation). The views are from below the pavement, looking NE.

to the fold axis. The stress tensors were obtained from veins affecting the Madison, Phosphoria and Tensleep formations in both limbs, except sample B12 collected in the syncline north of the NW fold termination (Figure 8). Most samples recorded a compressional stress regime, except three of them which yielded a strike-slip stress regime. In samples V1 and SMA7, the σ_1 axis is similarly oriented but the σ_3 axis is horizontal and perpendicular to the set II veins from which twin measurements were taken. This is in agreement with the interpretation of set II fractures by *Bellahsen et al.* [2006a]. In sample B12, both a compressional regime with σ_1 perpendicular to fold axis and an extensional regime with vertical σ_1 and σ_3 axis parallel to fold axis were obtained. The different tensors related to this stress regime are therefore linked by stress permutations: after back tilting, σ_1 is either vertical and associated with a NW–SE trending σ_3 (Figure 8, sample B12), or horizontal, with either σ_2 or σ_3 trending NW–SE (Figure 8, S32/S38, and Figure 8, V1 and SMA7). This suggests that NE–SW LPS2 was not a simple stress regime, varying both spatially and temporally throughout the fold from true NW–SE perpendicular extension to true NE–SW compression or a strike-slip regime with NE–SW compression and NW–SE extension. Such stress permutations are common during fold evolution. In the frame of the study, they can well account for the formation of set II veins from which twin data were collected and of associated LPS2 stylolites.

[51] A postfolding stage is also preserved by twinning in the veins and matrix from sandstones of the Tensleep Formation and carbonates from the Madison and Phosphoria formations, whatever the orientations of the veins from which measurements were taken. In all tensors the stress regime is strike-slip in type and the σ_1 axis strikes perpendicular to the fold axis (Figure 9).

[52] Extensional stress tensors were also identified (Figure 10). Three tensors were obtained from veins from

Table 2. Results of Stress Tensor Determination Based on Calcite Twin Data[a]

Sites	Formation	Age	Bedding Strike, Dip	Vein Strike, Dip	Trend (Plunge) of the Principal Stress Axes (deg) σ_1	σ_2	σ_3	$(\sigma_1 - \sigma_3)$ (MPa)	Ratio Between Differential Stress Φ	Total Number of Data T/UT	Number of Data Consistent With the Tensor T/UT
SMA1	Madison	Lower Carboniferous	117, 20 S	125, 80 NE	40 (57)	166 (21)	266 (24)	15 (±3)	0.5	82/23	42/16
					57 (76)[b]	169 (05)[b]	260 (13)[b]				
					223 (30)	322 (16)	76 (56)	23 (±5)	0.7	41/23	33/15
					221 (11)[b]	315 (23)[b]	109 (65)[b]				
SMA5	Tensleep	Upper. Carboniferous	146, 56 SW	120, 84 NW	62 (08)	266 (81)	152 (04)	44 (±9)	0.6	75/111	33/101
SMA7	Phosphoria	Permian	135, 32 SW	60, 85 NW	234 (34)	64 (55)	327 (05)	19 (±4)	0.6	114/24	54/24
					232 (02)[b]	127 (79)[b]	323 (11)[b]				
					46 (06)	264 (82)	136 (05)	43 (±9)	0.6	61/24	45/15
KAL4	Madison	Lower Carboniferous	137, 27S		312 (09)	67 (69)	219 (19)	43 (±9)	0.5	231/66	87/54
					308 (06)[b]	182 (80)[b]	39 (08)[b]				
					251 (07)	348 (46)	154 (43)	26 (±6)	0.2	150/66	58/59
KAL18	Madison	Lower Carboniferous	139, 52 NE		64 (18)	185 (58)	325 (26)		0.1	231/39	143/27
					321 (31)	199 (42)	73 (32)	13 (±3)	0.4	91/39	64/30
					345 (17)[b]	120 (67)[b]	250 (17)[b]				
B12	Thermopolis	Cretaceous	0, 0		13 (02)	104 (06)	268 (83)	70 (±14)	0.2	184/62	95/48
					95 (73)[b]	233 (13)[b]	326 (11)[b]	21 (±4)	0.7	92/62	36/52
B27	Phosphoria	Permian	127, 86 N		191 (54)	29 (34)	293 (09)	44 (±9)	0.5	47/36	25/29
					55 (36)[b]	206 (51)[b]	315 (14)				
					298 (14)	204 (17)	66 (68)	20 (±4)	0.5	93/36	46/25
					321 (10)[b]	81 (72)[b]	228 (15)				
V1	Phosphoria	Permian	136, 83 N	21, 70 E	45 (82)	225 (08)	135 (00)	45 (±9)	0.4	177/78	74/65
					226 (01)[b]	271 (89)[b]	136 (01)[b]				
					33 (19)	278 (51)	136 (33)	30 (±6)	0.3	102/78	49/70
V2	Phosphoria	Permian	136, 83 N	50, 30 E	195 (07)	104 (04)	342 (82)	51 (±10)	0.6	148/58	66/46
					134 (59)[b]	307 (31)[b]	39 (03)[b]				
					223 (19)	66 (69)	315 (08)	21 (±4)	0.8	102/58	40/54
B33	Phosphoria	Permian	136, 83 N		320 (05)	229 (11)	72 (78)		0.1	160/38	104/29
					141 (03)[b]	10 (85)[b]	231 (04)[b]				
					236 (32)	53 (57)	145 (01)	36 (±7)	0.9	56/38	34/38
S37_8	Tensleep	Upper Carboniferous	145, 39 SW	57, 84 SE	251 (40)	351 (12	95 (47)	25 (±5)	0.5	104/79	36/72
					247 (02)[b]	338 (26)[b]	152 (64)[b]				
S38_1	Phosphoria	Permian	146, 56 SW	120, 84 S	204 (39)	307 (15)	54 (47)	18 (±4)	0.8	67/66	27/64
					31 (11)[b]	123 (07)[b]	242 (77)[b]				
S32_11	Phosphoria	Permian		100, 74 N	193 (80)	293 (02)	23 (09)	44 (±9)	0.6	178/83	78/73
					21 (16)[b]	112 (03)[b]	211 (75)[b]				
FLC 2	Madison	Lower Carboniferous	150, 42 NE	150, 70 SW	191 (54)	324 (26)	66 (22)	41 (±8)	0.3	192/69	99/61
					120 (59)[b]	344 (23)[b]	246 (20)[b]				

[a]Ratio Φ is defined in text. T/U, twinned/untwinned planes.
[b]Back-tilted stress axes.

sets I and III showing σ_3 axes nearly perpendicular to the fold axis. This extension possibly reflects outer rim extension close to or at the fold hinge. However, it cannot be excluded that some of these tensors may be linked to the 135° LPS1 stage through a permutation of σ_1 and σ_2 axes.

4.1.2. Paleostress Orientations From Fault Slip Data

[53] The main compressional event corresponds to an ENE–WSW to NE–SW trend, nearly perpendicular to the trend of SMA axis. It is marked in the field by prefolding and postfolding fault systems. The prefolding fault system consists of dominant reverse microfaults clearly tilted within the strata (Figures 5c and 5d). In the backlimb, the NE compression is marked by numerous stylolitic peaks oriented within the bedding and well observable in the canyon of the Bighorn River within the Madison Formation (Figures 5 and 8). In some places, the NE trend evolves to ENE in the overlying Tensleep sandstones. This prefolding faulting event corresponds to LPS2. In some sites, the low bedding dip precludes unambiguous recognition of the prefolding character of faulting (site X5); we chose however to relate them to LPS2.

[54] The second faulting event is also related to NE compression but mainly occurred after bed tilting, and likely reflects a late stage of fold tightening. Whereas LPS2 is rather marked by stylolites and reverse microfaults, this event is instead marked by mixed reverse and strike-slip faults. The mixed populations of reverse faults and strike-slip faults probably represent protracted deformational events where, because of slight changes in relative horizontal stress magnitudes, the vertical stress component at some

Table 3. Results of Strain Tensor Determination Based on Calcite Twin Data

Sites	Formation	Age	Bedding Strike, Dip	Vein Strike, Dip	Trend (Plunge) of the Principal Strain Axes (deg) ε_{min}	ε_{int}	ε_{max}	ε_{min} (%)	ε_{int} (%)	ε_{max} (%)	NEV[a] (%)
SMA1	Madison	Carboniferous	117, 20 S	125, 80 NE	24 (12)	160 (70)	301 (16)	−1.8	−0.2	2	31
KAL4	Madison	Carboniferous	137, 27S		306 (30)	182 (40)	58 (31)	−1	−1	2	39
					293 (22)[b]	192 (19)[b]	65 (57)[b]				
					84 (16)	338 (40)	193 (44)	−0.5	0	0.5	22
KAL18	Madison	Carboniferous	139, 52 NE		34 (10)	155 (68)	301 (13)	−3	1	2	25
B12	Thermopolis	Cretaceous	0, 0		31 (06)	118 (05)	192 (83)	−2	0	2	21
B27	Phosphoria	Permian	127, 86 N		119 (13)	3 (59)	227 (22)	−0.75	−0.25	1	16
					293 (07)[b]	199 (21)[b]	10 (70)[b]				

[a]NEV, negative expected values (see text).
[b]Back-tilted strain axes.

times and places represents σ_2 and at other times and places within the fold represents σ_3. Therefore, these minor faults do not appear to be the result of more than one general period of deformation, but the relative values of stresses probably varied during folding, leading to local stress permutations between σ_2 and σ_3. These late strike-slip and reverse faults clearly offset subvertical strata and earlier fault sets in the forelimb (Figures 5f and 5j); some of the

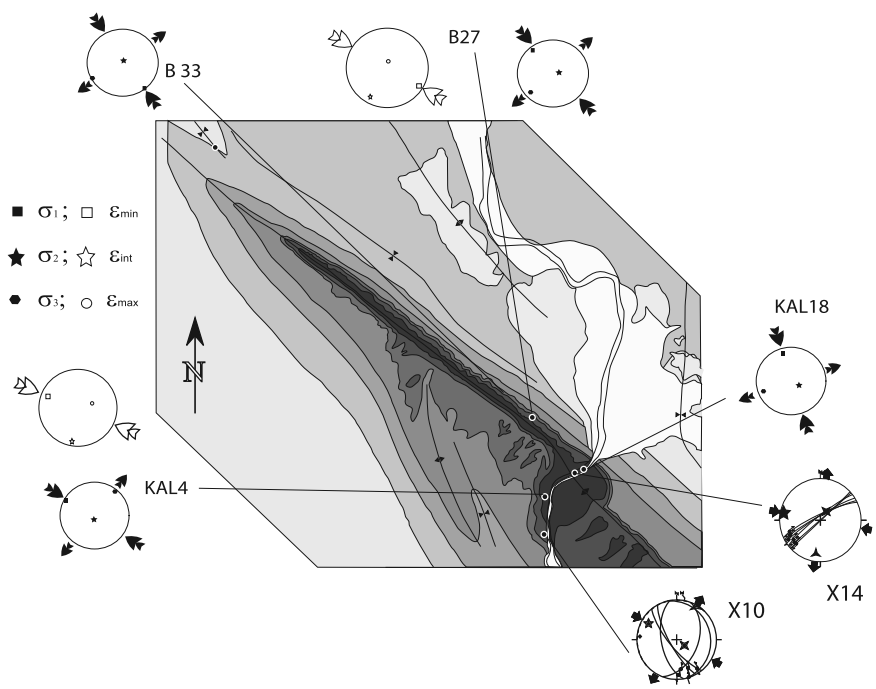

Figure 7. Paleostress orientations related to Sevier LPS1 derived from faults and calcite twins. Diagrams illustrating calcite twin data: thin curves represent vein planes. Solid squares, stars, and circle indicate the principal stress axes (σ_1), (σ_2), and (σ_3), respectively. Open squares, stars, and circle indicate the principal strain axes (ε_{min}), (ε_{int}), and (ε_{max}), respectively. Black arrows indicate directions of compression (convergent arrows) and extension (divergent arrows). White arrows indicate direction of shortening (convergent arrows) and traction (divergent arrows). All the diagrams are shown in the back-tilted attitude. In the diagrams illustrating fault slip data, thin curves represent fault planes and dots with double arrows (left- or right-lateral) or simple ones (centripetal-reverse/centrifugal-reverse) indicate striations. Stars indicate stress axes with five points (σ_1), four points (σ_2), and three points (σ_3). Small black diamonds represent stylolitic peaks. Large black arrows indicate direction of compression (convergent arrows) and extension (divergent arrows). All the diagrams are shown in the back-tilted attitude.

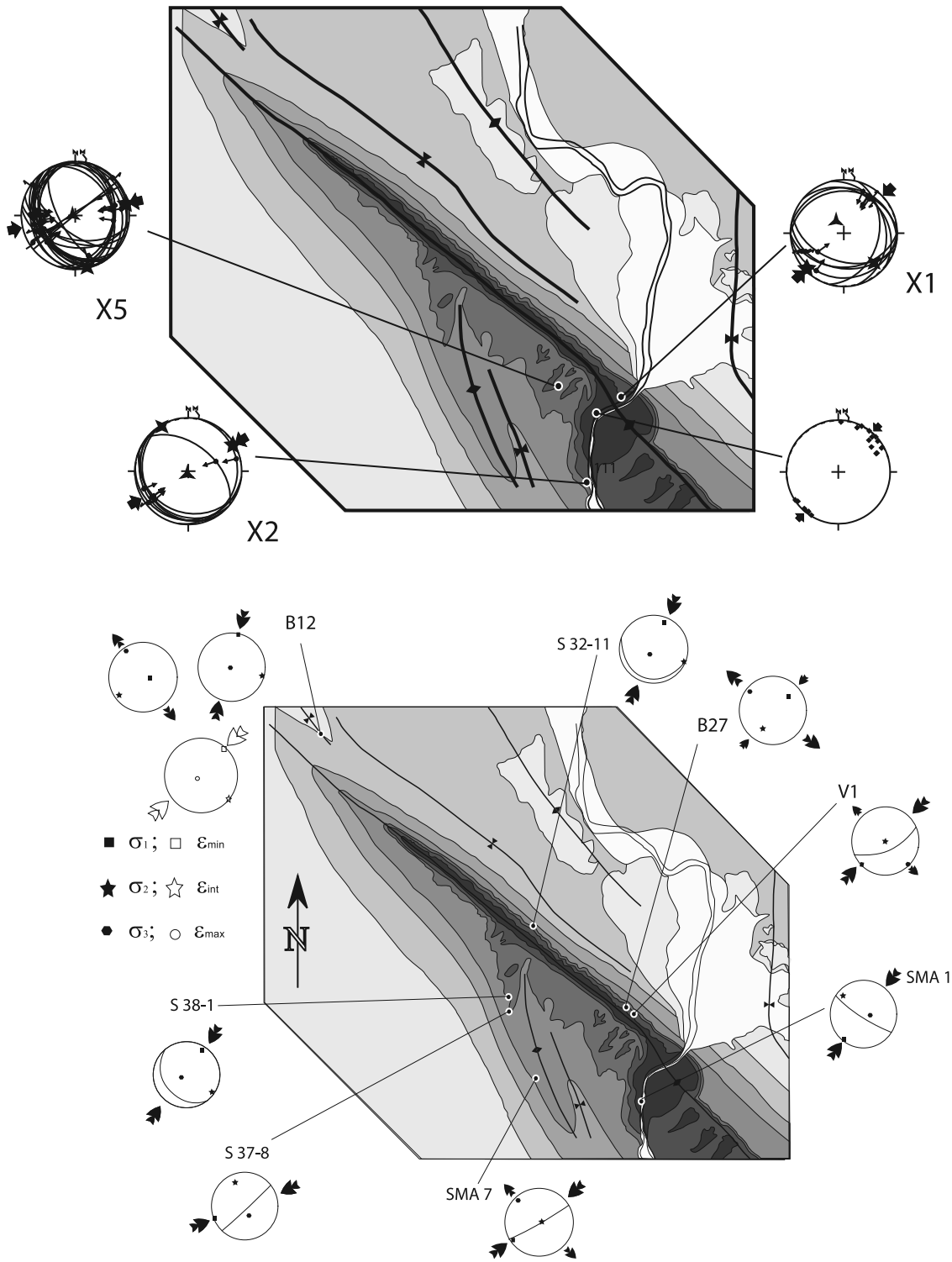

Figure 8. Paleostress orientations related to Laramide LPS2 derived from faults and calcite twins. For the diagrams illustrating calcite twin data and fault slip data, key is the same as in Figure 7. All the diagrams are shown in the back-tilted attitude.

late reverse faults correspond to reactivated set I fractures (Figure 5i). This late fold tightening stage seems to be better represented in the forelimb, but this may also be due to more favorable outcropping conditions due to bedding dip. These reverse faults are consistent with previous observations by *Hennier and Spang* [1983] and *Forster et al.* [1996]. Bed-parallel slip planes with slickensides [*Hennier and Spang*, 1983; *Sanz et al.*, 2008], mostly observed in the

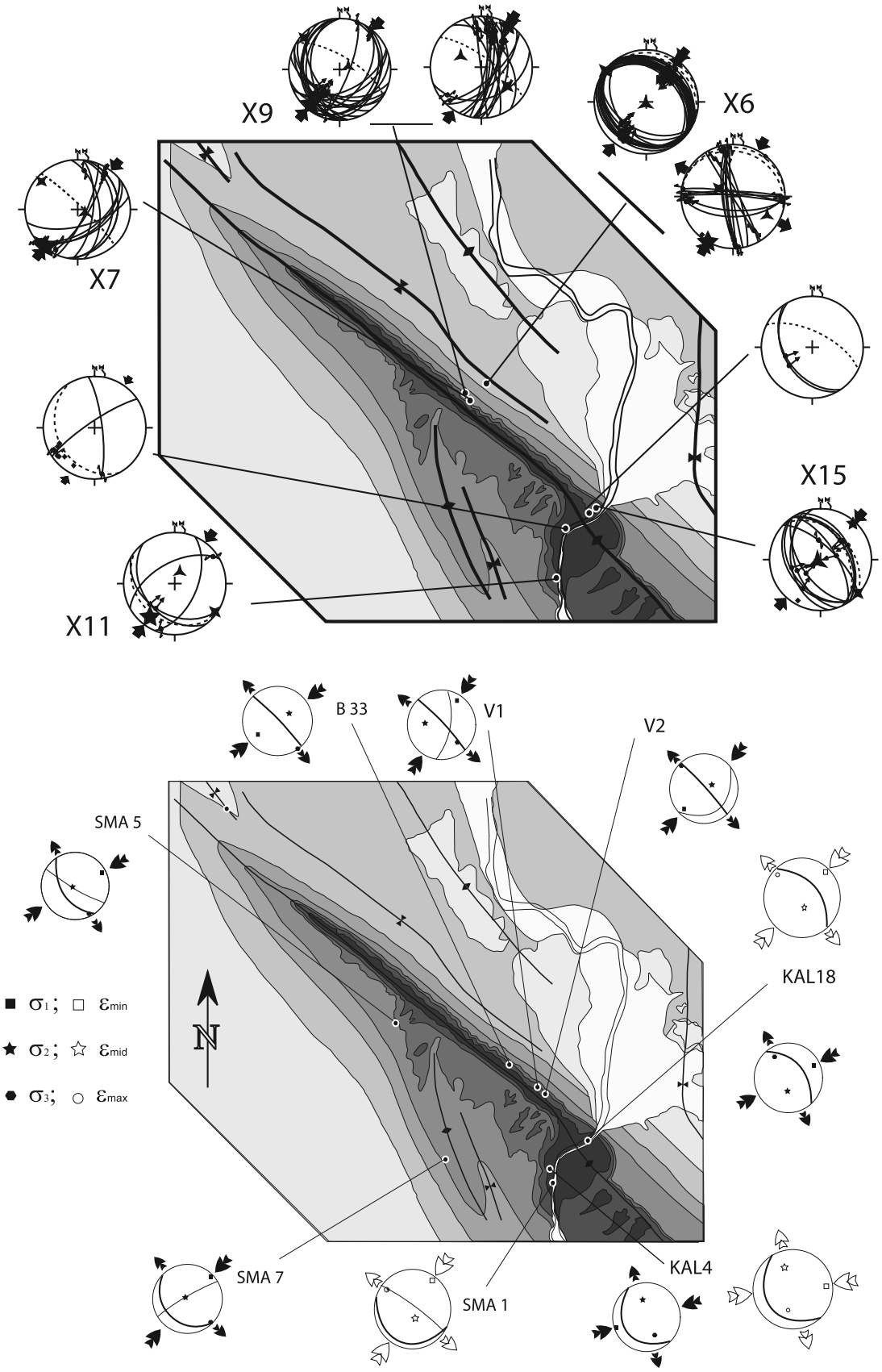
X9
X6
X7
X15
X11
B 33
V1
V2
SMA 5
KAL18
N
σ1 ; εmin
σ2 ; εmid
σ3 ; εmax
SMA 7
SMA 1
KAL4

Figure 9

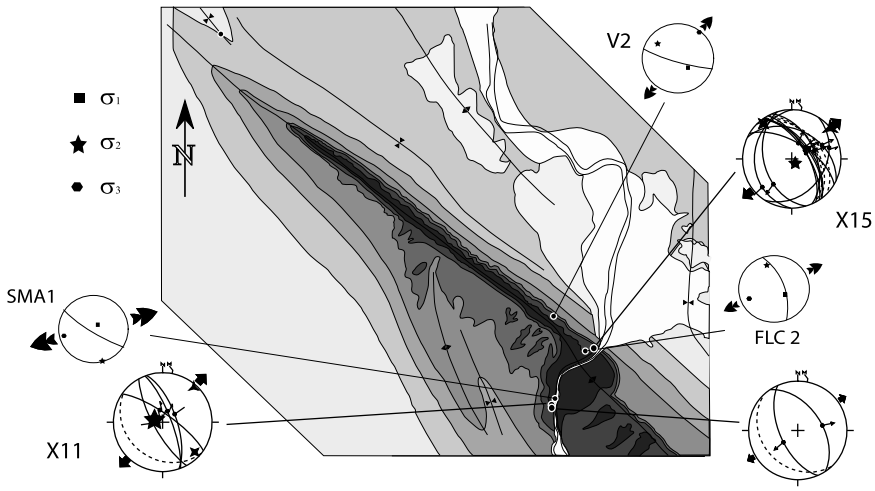

Figure 10. Extensional stress tensors with σ_3 axis normal to fold axis derived from faults and calcite twins. For the diagrams illustrating calcite twin data shown in the back-tilted attitude, key is the same as in Figure 7. For the diagrams illustrating fault slip data, key is the same as in Figure 7. Bedding planes (in their present attitude) shown as dashed lines.

forelimb, indicate a component of flexural slip with slip directions approximately normal to the fold axis and support a NE directed transport. This main NE–SW compression is also clearly recorded by conjugate systems of reverse and strike-slip faults in the nearly flat-lying Cretaceous limestones of the syncline north of SMA (Figure 9).

[55] A normal faulting stress regime associated with a NE–SW direction of extension has also been identified in few sites within the Bighorn River canyon, in the hinge and the steeply dipping forelimb. It is marked by steeply dipping normal faults striking parallel to SMA axis.

[56] A prefolding NW–SE compression event has also been recognized. Well documented by calcite twinning, this event is instead poorly marked by microfaults. Only 2 sites (Figure 7) show evidence for microfaulting to mesofaulting related to this compression trend (Figure 5k).

4.1.3. Successive Fracture Sets and Related Paleostresses

[57] Our new fracture analysis reveals the same first-order picture of development of successive fracture sets than the previous studies by *Bellahsen et al.* [2006a] and *Fiore* [2006] but additionally allows refining some of their conclusions. The set I fractures defined by *Bellahsen et al.* [2006a] were striking 110°E. As reported in Figure 11, those fractures actually range in strike between 110°E and 140°E (Figure 11, for example: sites 73, 74, 82). In the field, they are observed in many places as predating all the other fractures. Taking into account the NW–SE LPS1 trend derived from faults and calcite twins, we argue that these fractures most probably consist of pre-Laramide mode I fractures likely related to Sevier far-field orogenic stresses. These fractures were subsequently sheared during Laramide times [*Bellahsen et al.*, 2006a]: in the forelimb, they were reactivated as late folding thrust faults (Figure 5i), while they were reactivated as strike-slip faults in the backlimb as shown by associated tail cracks [*Fiore*, 2006].

[58] Our study also points out N–S trending and N045° trending fracture sets in the forelimb of SMA. The N–S set was not interpreted by *Bellahsen et al.* [2006a], and they argued that the LPS2-related 045°E joint set (set II) was significantly missing in the forelimb. Our new observations show that set II joints and veins that mark the NE compression can also be recognized in the forelimb, although they are less numerous there than in the backlimb and the hinge; they additionally show significant reorientation (local trends of 060–070°, Figure 11, sites 11, 32, 58 for example). The N–S fractures, more abundant in the forelimb than in the backlimb, were observed in other places around the Bighorn basin [*Callot et al.*, 2008]. Where chronological observations are reliable, they appear to predate 045°E fractures (Figure 6a) (J.-P. Callot, personal communication, 2009), and likely predate the Laramide folding event. Their tectonic significance still remains unclear.

[59] Finally, still in the forelimb, we observe fracture trending E-W in unfolded position (and 020°E east dipping in the present-day position). These previously undescribed fractures clearly postdate set II fractures (045°E, Figure 6b). As set II fractures probably initiate at the very beginning of folding (prefolding to early folding LPS2), these latter fractures probably occurred during the folding event. Thus, they might be interpreted as due to local extensional stresses, layer-parallel and in a plane close to vertical. Their occurrence may reflect a first stage of fold development with a large hinge including part of the future forelimb that has later migrated through time and/or localized in the present hinge.

Figure 9. Paleostress orientations related to Laramide late stage fold tightening derived from faults and calcite twins. Diagrams illustrating calcite twin data and fault slip data. same key as in Figure 7. Bedding planes (in their present attitude) shown as dashed lines.

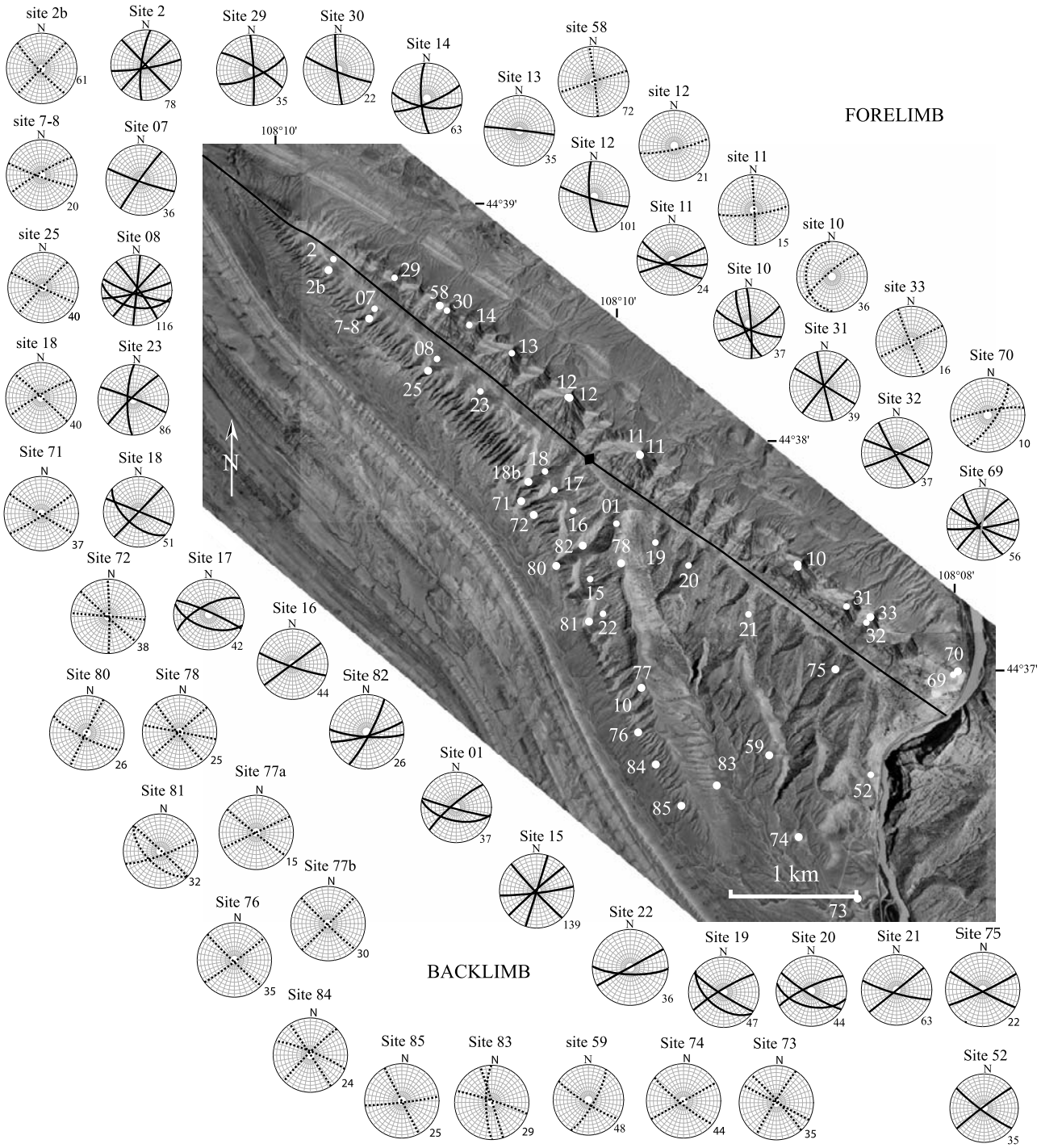

Figure 11. Aerial photograph of SMA with the backlimb, forelimb, and hinge fracture measurement sites and corresponding polar stereonets. Great circles represent the average bedding-corrected orientations of fracture sets. Dotted lines are for fracture data collected in the Phosphoria Formation.

4.2. Finite Strain Orientations and Magnitudes From Calcite Twins

[60] The five samples analyzed with Groshong's CSGT [*Groshong*, 1972] (Figures 7–9) also reveal three stages of finite strain. NW–SE LPS1 is preserved by twinning in Kal.4 in the backlimb and in B27 in the forelimb, with a small ε_{min} ($\sim-1\%$). These strain tensors are purely contractional with ε_{max} perpendicular to bedding (Figure 7). NE–SW directed LPS2 is preserved in matrix from sample B12 which recorded a ε_{min} equal to -2% and a ε_{max}

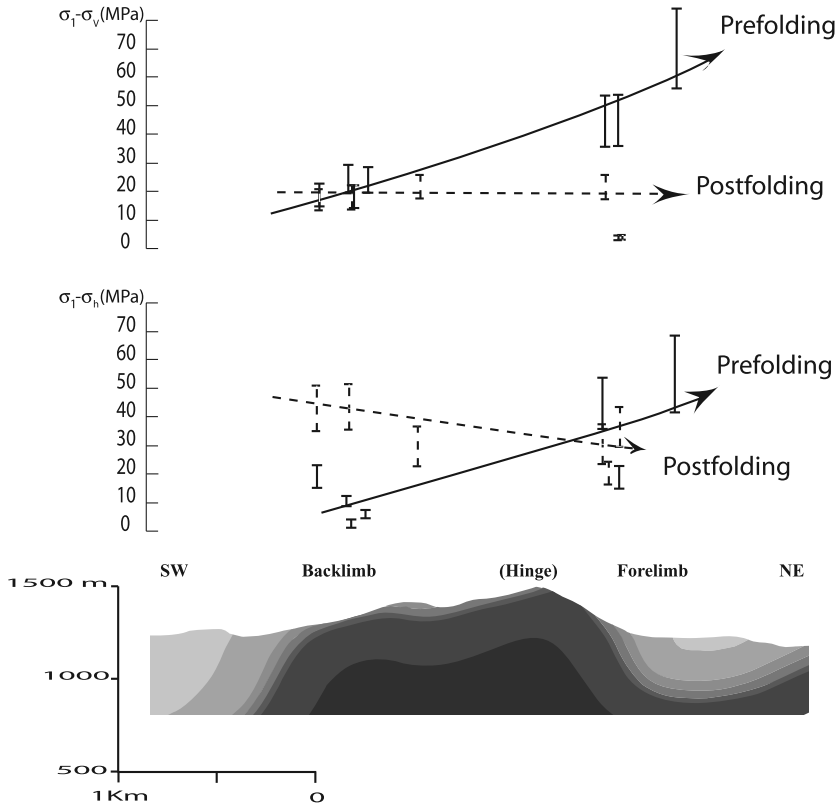

Figure 12. Evolution of Laramide prefolding and postfolding differential stresses through SMA (sites projected perpendicularly on the cross section of Figure 3).

perpendicular to bedding and vertical (Figure 8). Finally, samples Kal.18, Kal.4 and SMA.1 yield a strain tensor with ε_{min} perpendicular to the fold axis in the present-day attitude, suggesting that calcite twinning in these samples mainly recorded late stage fold tightening; ε_{max} is horizontal and parallel to the fold axis. ε_{min} values vary between −1.8 and −3% (except for Kal 4, Table 3).

4.3. Paleodifferential Stress Magnitudes Related to Folding in SMA

[61] As mentioned above, calcite twin analysis reveals a dominant prefolding compressional regime and a dominant postfolding strike-slip stress regime related to the Laramide tectonism. In order to properly compare Laramide differential stress values both in space (backlimb versus forelimb) and time (prefolding versus postfolding), and to take into account local (σ_2/σ_3) stress permutations, we have reported the curves showing the evolution of ($\sigma_1 - \sigma_v$) and ($\sigma_1 - \sigma_h$) rather than ($\sigma_1 - \sigma_3$) and ($\sigma_1 - \sigma_2$) curves (Tables 2 and 3 and Figure 12). During Laramide LPS2, both ($\sigma_1 - \sigma_v$) and ($\sigma_1 - \sigma_h$) increased from the backlimb toward the forelimb. ($\sigma_1 - \sigma_v$) increases from nearly 20 MPa in the backlimb to a value ~60 MPa in the forelimb while ($\sigma_1 - \sigma_h$) evolves from 10 MPa in the backlimb to ~50 MPa in the forelimb. A nearly similar increasing trend is therefore documented for ($\sigma_1 - \sigma_v$) and ($\sigma_1 - \sigma_h$) during Laramide LPS.

[62] During late stage fold tightening, ($\sigma_1 - \sigma_v$) remains nearly constant around 20 MPa in the backlimb and the forelimb. ($\sigma_1 - \sigma_h$) decreases from more than 40 MPa in the backlimb to nearly 20 MPa in the forelimb.

[63] Although the uncertainties on these estimates are rather large (±20%, see section 3.1.1; "error bars" on Figure 12), the overall trends of variation of these values (increasing or decreasing trends) and relative proportions of these estimates are reliable and can be used for discussion.

5. Discussion

5.1. Consistency of Stress and Strain Orientations and Regimes From Faults and Calcite Twins

[64] This study constitutes the first attempt to use jointly Etchecopar's CSIT and Groshong's CSGT to derive both stress and calcite strain prior to, during and after folding from a single set of samples. The weak calcite twinning strain (<3%) allows a direct comparison between finite strain tensors and stress tensors.

[65] In terms of orientations of shortening ε_{min}/compression σ_1, the results show a very good consistency, for the two LPS stages and the late stage fold tightening, therefore supporting that internal strain of folded strata remained mainly coaxial. The stress regimes and the regime of deformation for the prefolding and postfolding NE–SW

compression are consistent (mainly purely compressional for LPS2 and of strike-slip type with $\varepsilon_{max}/\sigma_3$ nearly horizontal for late stage fold tightening). However, for the NW–SE directed compression (LPS1), the regime is dominantly strike slip in term of stress and dominantly compressional in terms of strain. Comparisons between Laramide stress regimes derived from calcite twins with those derived from fault slip data shows a good agreement in both stress orientations and regimes. For the postfolding NE compression, the stress tensors determined from calcite twins are clearly of strike-slip type while those revealed by fault slip analysis are rather compressional strike-slip (σ_3 vertical but Φ ratios equal or close to 0 for sites X7, X9 and X11, Table 1). This is confirmed by the postfolding compressional reactivation of set I veins (Figure 5i) and the offset of subvertical bedding by late strike-slip faults (Figure 5f) in the forelimb.

[66] A major result of this study is therefore that prefolding stresses and stresses related to fold development were recorded homogeneously at different scales, i.e., from the microscopic (grain/aggregate) scale to the macroscopic (fracture sets) scale, therefore demonstrating that the whole stress history can be reliably deciphered from local observations.

5.2. Chronology of Successive Twinning Strains and Stresses and Regional Significance of Reconstructed Twinning Events

[67] In SMA, all the stress-strain indicators reveal a polyphase tectonic evolution. This is for instance clearly evidenced by sample KAL4 which revealed a NW–SE (Sevier) and an ENE–WSW (Laramide) shortening-compression trends using both Groshong's and Etchecopar's techniques (Figures 7, 8, and 9). Some samples have also preserved stress tensors related to the Laramide LPS2 and to late stage fold tightening, which could be revealed only using Etchecopar's technique (e.g., sample SMA7).

[68] The chronology of successive twinning strains and stresses is based first on the observation that some strain-stress tensors have maximum shortening-compression axes ($\varepsilon_{min}/\sigma_1$) inclined consistently and with the same dip as the bedding, while some others have maximum shortening-compression axes that are horizontal irrespective of bedding dip (section 3.4). This leads us to clearly distinguish LPS-related strain-stress tensors to strain-stress tensors related to late stage fold tightening [e.g., *Harris and van der Pluijm*, 1998; *Lacombe et al.*, 1996a, 2007]. There is no clear evidence for strain-stress tensors with maximum shortening-compression axes inclined consistently less than, but in the same direction as bedding dip which would have reflected either synfolding twinning [*Lacombe*, 2001] or rotation of prefolding twins at the grain scale due to flexural slip [*Harris and van der Pluijm*, 1998].

[69] The chronology between successive twinning strains and stresses is further based on the comparison of calcite twinning strains and stresses preserved in rock matrix and in the successive vein sets. A stress tensor determined from the calcite grains filling a vein with a σ_3 axis perpendicular to the vein strike is likely related to the vein formation while other tensors (with stress axes inconsistent with the vein geometry) reflect later, postopening stress regimes (e.g., LPS2 recorded in set I vein at site SMA1). To this respect, the Sevier LPS1 was recorded by twinned calcite in the rock matrix, while the Laramide-related LPS2 was recorded in both the matrix and the veins, especially in set I and set II veins (Figure 8). The late stage fold tightening was recorded in both the matrix and the veins irrespective of their orientation (Figure 9). This strengthens the proposed relative chronology of successive stress regimes, with a first record of far-field Sevier stresses, mostly strike-slip, followed by the record of Laramide stresses, mostly compressional. Note that a vein attributed to the latest set IV by *Bellahsen et al.* [2006a] (SMA5, Figure 9) recorded the postfolding Laramide stresses, which means that these latest veins may have developed while the fold was still submitted to Laramide compression.

[70] This criterion of preservation of calcite twinning strain either in the matrix or in the veins is similar to that reported by *Craddock and van der Pluijm* [1999] to infer relative chronology between Sevier-related LPS1 and Laramide-related LPS2. The direction of regional LPS calcite fabric in the carbonate country rocks is oriented ENE–WSW and is considered to be Sevier-related, while synorogenic calcite cements and veins preserve a subhorizontal, N–S shortening strain, regardless of the vein orientation, related to Laramide shortening (Figure 1a). In SMA, the NW–SE trend can therefore be related to the far-field Sevier orogenic stresses for the period 80–75 Myr (Late Cretaceous: Campanian [*Bird*, 1998]).

[71] Our study therefore yields a stress history consistent with previously reported stress trends in the area investigated and surroundings (Figure 1). In particular, the main Laramide NE (to ENE) compressional trend identified in SMA is consistent with NE trending slickensides reported along the Five Springs thrust by *Hoppin* [1970] and with Laramide stress tensors derived by *Wise and Obi* [1992] in the same area, and with the ENE to NE trend of the regional compression during the Laramide orogeny [*Sales*, 1968; *Reches*, 1978; *Brown*, 1988; *Varga*, 1993; *Bird*, 2002; *Neely and Erslev*, 2009]. In the absence of positive evidence of successive distinct Laramide compressional trends in our new results, we follow *Varga*'s [1993] conclusion that around the Bighorn basin, the dominant Laramide compressional trend remained almost NE–SW and that local deviations may have arisen from strain partitioning with zones of dominantly compressional deformation and zones of dominantly strike-slip faulting along structures strongly oblique to the overall Laramide compression.

[72] The increase of calcite twinning shortening between Sevier LPS1 ($\sim-1\%$) and Laramide late stage fold tightening ($\sim-3\%$) (Table 3) can be tentatively explained by considering the more westward location of the Sevier deformation front compared to Laramide front. A similar interpretation was made by *Silliphant et al.* [2002] at Split Mountain in Utah and *Hennings et al.* [2000] at Oil Mountain in Wyoming. Therefore, the mean calcite twinning strain in our samples reliably reflects the relative amount of regional

deformation related to these two tectonic phases in the area of interest. This study therefore highlights the potential of calcite twin analyses to yield a representative picture of successive regional/local stress and strain patterns.

5.3. Comparison With Fracture Data

[73] LPS2-related stress inferred from subvertical set II fractures is of strike-slip type [*Bellahsen et al.*, 2006a]. Although found in place in the forelimb, this fracture set was mainly described in the backlimb, a geographic dependence which was tentatively related to local stress perturbations in the forthcoming forelimb at the tip of the underlying high-angle thrust which may have prevented formation of vertical extensional fractures perpendicular to fold axis [*Bellahsen et al.*, 2006b]. Our results suggest that set II fractures are also present in the forelimb and that LPS2 in both the forelimb and the backlimb was also marked by reverse faulting and stylolitization. This suggests that the stress field related to Laramide LPS2 was probably more complex than previously thought, evolving between strike-slip and reverse in type through σ_2/σ_3 permutations, with a nearly constant NE horizontal paleo-σ_1 trend.

[74] A major point deals with the recognition of a pre-Laramide horizontal compression in the SMA area, which is a matter of debate (E. A. Erslev, personal communication, 2009). Prefolding set I joints predating all other fractures (Figure 11), microfaults and stylolites (Figure 7) as well as LPS1-related twinning (Figure 7) consistently support the actual occurrence of a NW-SE compressional trend and associated perpendicular extension in pre-Laramide times in SMA. The NW–SE trend revealed by twinning corresponds mainly to a strike-slip mode consistent with the trend of set I joints and veins ranging from N110° [*Bellahsen et al.*, 2006a, 2006b] to 130°–140° [*Fiore*, 2006; this study].

[75] The interpretation of the NW striking set I joints and veins as pre-Laramide seems to disagree with observations made elsewhere in the Rockies (E. A. Erslev, personal communication, 2009). This author challenges the assumption that layer-perpendicular joints formed prior to folding since bedding anisotropy may reorient stresses in this direction for a wide range of bedding dips; he especially argues that there is no evidence of pre-Laramide jointing in the Bighorn Basin and that NW striking joints are instead postfolding. Our interpretation of set I joints and veins as pre-Laramide is however not only based on their bed-perpendicular attitude. Several lines of evidence support the formation of this set before Laramide folding. First, Laramide LPS2-related set II veins clearly abut on the set I veins, as already reported by *Bellahsen et al.* [2006a]. Second, stylolites oriented NE–SW with peaks oriented N110° to N135° were observed: they not only support that set I veins likely formed under NW compression and splitting rather by simple horizontal extension, but when observed in thin section, one of these stylolites has been found reopened by a set II vein, on which a set III vein abuts [*Beaudoin*, 2009]. Third, set I joints and veins show evidence of left-lateral shear reactivation during Laramide compression in the backlimb of SMA, while they were reactivated as reverse faults in the forelimb after folding (Figure 5i). Finally (see section 4.1.1), calcite from a N110° striking vein (set I) recorded Laramide LPS2 with a σ_1 axis perpendicular to the vein (site SMA1, Figure 8). These chronological observations lead us to conclude that set I joints and veins likely predate Laramide tectonism. They further allow to distinguish these early fractures from the also 135°E trending, synfolding set III joints that are mainly present in the hinge.

[76] Although normal faults developed after folding (Figure 10), both their trends and their extensional nature are consistent with occurrence of set III fractures and possibly in response to bending stresses during folding. Two interpretations can however be proposed. According to the first one, postfolding normal faults and prefolding calcite twin sets, both related to NE extension perpendicular to fold axis, are related to overall outer rim extension also marked by set III veins. In the second one, neither the extensional twin sets nor the normal fault sets are related to outer rim extension which is only marked in the field by set III veins; in this case the NE extension revealed by calcite twinning may be related to the N135° LPS1 episode through stress permutations, while late normal faults reflect post-folding, exhumation-related stress relaxation and in that sense may be correlated with the set IV joints.

5.4. Evolution of Stress Magnitudes During Folding Above a Basement Thrust Fault

5.4.1. Modeling of LPS2 Stresses in the Sedimentary Cover Above a Basement Thrust Fault

[77] In order to model the increasing trend of differential stresses ($\sigma_1 - \sigma_v$) and ($\sigma_1 - \sigma_h$) related to Laramide LPS2 from the backlimb to the forelimb of SMA (Figure 12), we performed a simple mechanical simulation of SMA fold development with the same geometry and kinematics as in the work by *Bellahsen et al.* [2006b] (Figure 13). This new modeling is carried out using Poly3D [*Thomas*, 1993], a three-dimensional boundary element program based on the displacement discontinuity method and the governing equations of linear elasticity. Single slip events or a series of events are considered with a complete stress relaxation occurring between each event. Linear elasticity is well suited for our study since we want to focus on the very first steps of deformation caused by the early motion along the thrust fault.

[78] The underlying fault at Sheep Mountain is interpreted as a SW dipping (Figure 13, around 50°) basement fault [*Stanton and Erslev*, 2004]. The boundary conditions are set as follows: the three principal stresses increase with depth as a result of the effect of burial. The most compressive stress is perpendicular to the fault (about 100 MPa at 2200 m deep) and the least compressive one is vertical (about 60 MPa at 2200 m depth). The intermediate principal stress is about 75 MPa at 2200 m depth. The density is set to 2700 kg/m^3. Young's modulus is set to 10 GPa, Poisson's ratio to 0.25.

[79] Modeling results (Figure 13) show that slip along the discontinuity induces stress perturbations around the fault tip. These stress perturbations occur both in orientations and magnitudes, in agreement with previous works [e.g., *Petit*

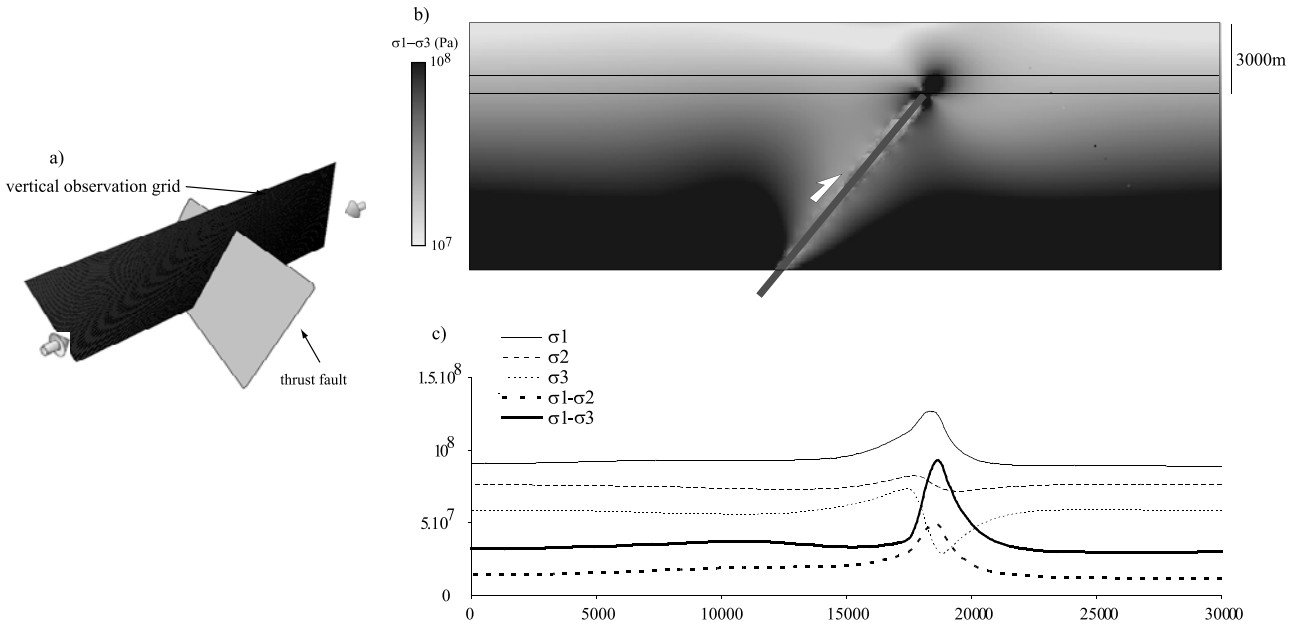

Figure 13. (a) Simple elastic model of stress distribution in a cover above a basement thrust fault. The stress regime is compressional (σ_3 vertical). (b) The stress magnitudes are those of (σ_1-σ_3). (c) The curves correspond to principal stress magnitudes σ_1, σ_2, and σ_3 and differential stresses (σ_1-σ_2) and (σ_1-σ_3) at 2200 m depth in the model.

and Barquins, 1988; *Homberg et al.*, 1997; *Bellahsen et al.*, 2006b]. However, because the model is basically elastic, the magnitudes of the perturbations of both stress orientations and values cannot be directly compared to our results. Especially, our calcite twin results do not support any large deviation of stress orientations from the vertical or the horizontal directions (taking into account the 10°–15° uncertainties on computed stress orientations). We therefore implicitly assume that directional deviations of the principal stress axes are low and do not preclude considering that σ_v remains a principal stress during fold evolution. In the following we only focus on the increasing or decreasing trends of differential stress magnitudes predicted by the model, to be compared with increasing or decreasing trends of differential stress magnitudes revealed by calcite twinning paleopiezometry (Figure 12).

[80] Figure 13 shows that the most compressive principal stress (horizontal, perpendicular to the fault in strike) is higher above the fault tip. The least (vertical) and intermediate compressive stresses are higher in the fault hanging wall. The differential stress values are also perturbed: $(\sigma_1 - \sigma_3)$ and $(\sigma_1 - \sigma_2)$ also increase when approaching the fault tip and reach a maximum above the fault tip. This result suggests that SMA backlimb was located in the hanging wall of (above) the reactivated fault and that the forelimb is located within its footwall very close above the fault tip (Figure 3). Note however that the forelimb is in the hanging wall of the developing short-cut thrusts (Figures 3 and 13).

[81] Thus, this simple model accounts for the first-order increase of differential stresses derived from calcite twins within the folded cover of SMA. It therefore supports the idea that the increase of prefolding differential stresses from the backlimb toward the forelimb could be related to the stress perturbation induced in the overlying cover by the tip of the underlying thrust fault that did not propagate (at least at the very beginning) within the cover.

[82] Our data further suggest that after motion along the basement thrust fault and fold development, stresses relaxed in the forelimb and that the differential stresses decreased near the thrust fault. In contrast, differential stress magnitudes keep on increasing in the backlimb, but the simple model used is unable to model stresses during fold evolution.

5.4.2. Tentative Scenario of Evolution of Principal Stresses Related to Folding in SMA

[83] On the basis of differential stress values derived from calcite twin analysis and of the results of the numerical simulations, we propose a tentative scenario of the evolution of principal stresses during folding in SMA (Figure 14). This scenario accounts for all the constraints derived from differential stress values from calcite twinning (Figure 12) as well as for the outputs of the numerical model about the evolution of principal stresses on both sides of the high-angle thrust. In particular, σ_v was found to largely increase in the hanging wall of the thrust fault compared to the footwall, while σ_h shows a much lower change across the fold (Figure 13). As mentioned in Section 5.4.1, we further consider that σ_v remains a principal stress during fold evolution. Note finally that in this scenario, the pore fluid pressure is not taken into account.

5.4.2.1. Spatial Changes (From Backlimb to Forelimb)

[84] During LPS2, $(\sigma_1 - \sigma_v)$ and $(\sigma_1 - \sigma_h)$ increase from the backlimb to the forelimb (Figure 12). According to the mechanical model, σ_v is much higher in the backlimb than in the forelimb due to stress perturbation, and σ_h shows little variations (Figure 13). The value of σ_1 increases toward the forelimb.

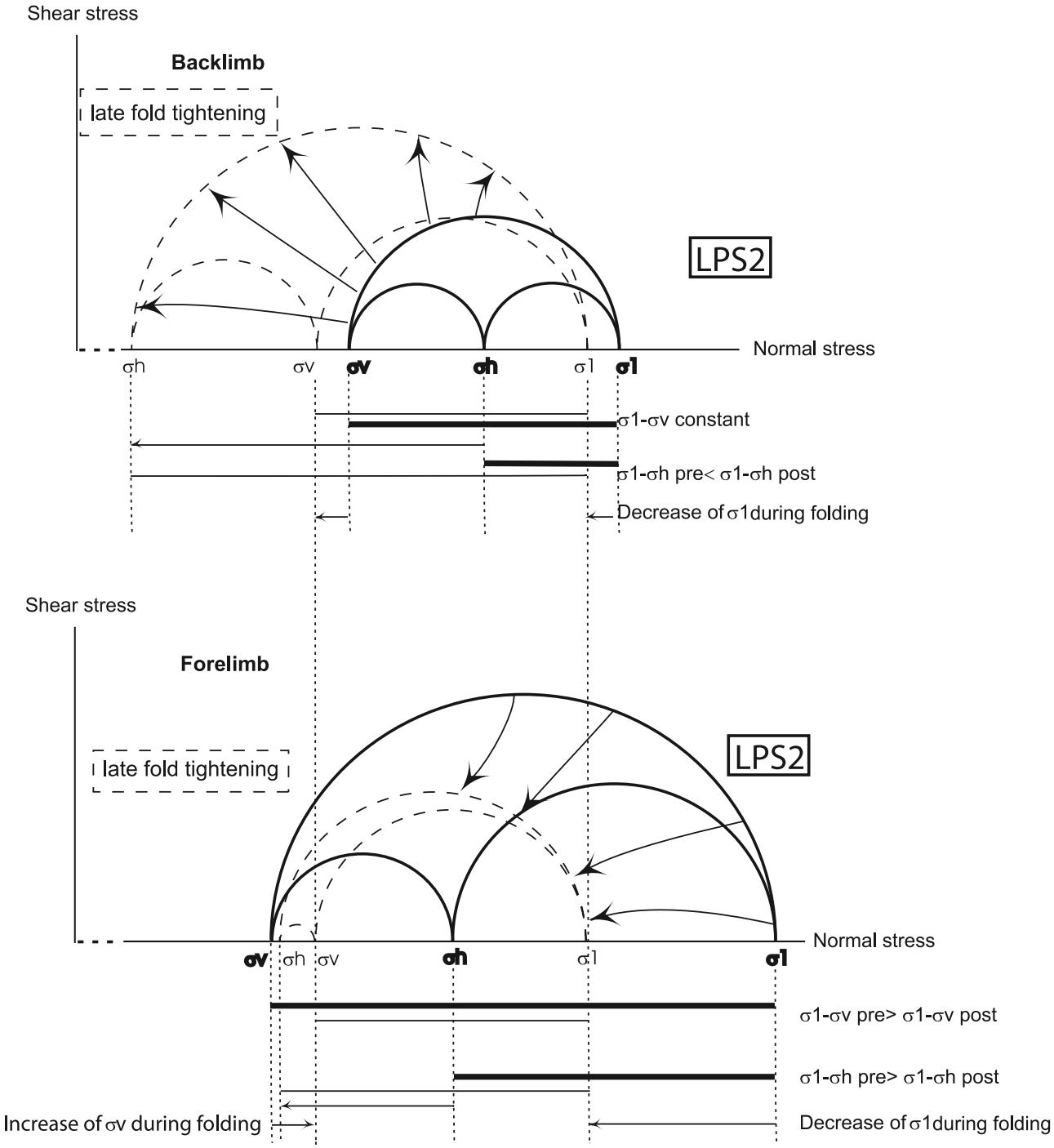

Figure 14. Tentative Mohr construction describing possible evolution of principal stress magnitudes across the anticline prior to and just after folding.

[85] During late stage fold tightening, $(\sigma_1 - \sigma_v)$ remains nearly constant through the fold (Figure 12). Assuming relaxation of the stress perturbation at fault tip during folding, the σ_v during the postfolding stage can be considered constant in the backlimb and the forelimb; the σ_1 remains therefore nearly the same in the backlimb and the forelimb. The decrease of $(\sigma_1 - \sigma_h)$ (Figure 12) implies an increase of σ_h toward the forelimb (Figure 14).

5.4.2.2. Change Through Time

[86] From LPS stage to the late stage fold tightening, $(\sigma_1 - \sigma_v)$ remains constant in the backlimb, but σ_v switched from σ_3 to σ_2 (i.e., change from reverse to strike-slip stress regimes, recorded by both twins and faults). The expected relaxation of the stress perturbation at fault tip during folding leads to a presumable slight decrease of $\sigma_{v,}$ even in the absence of significant synfolding erosion, which

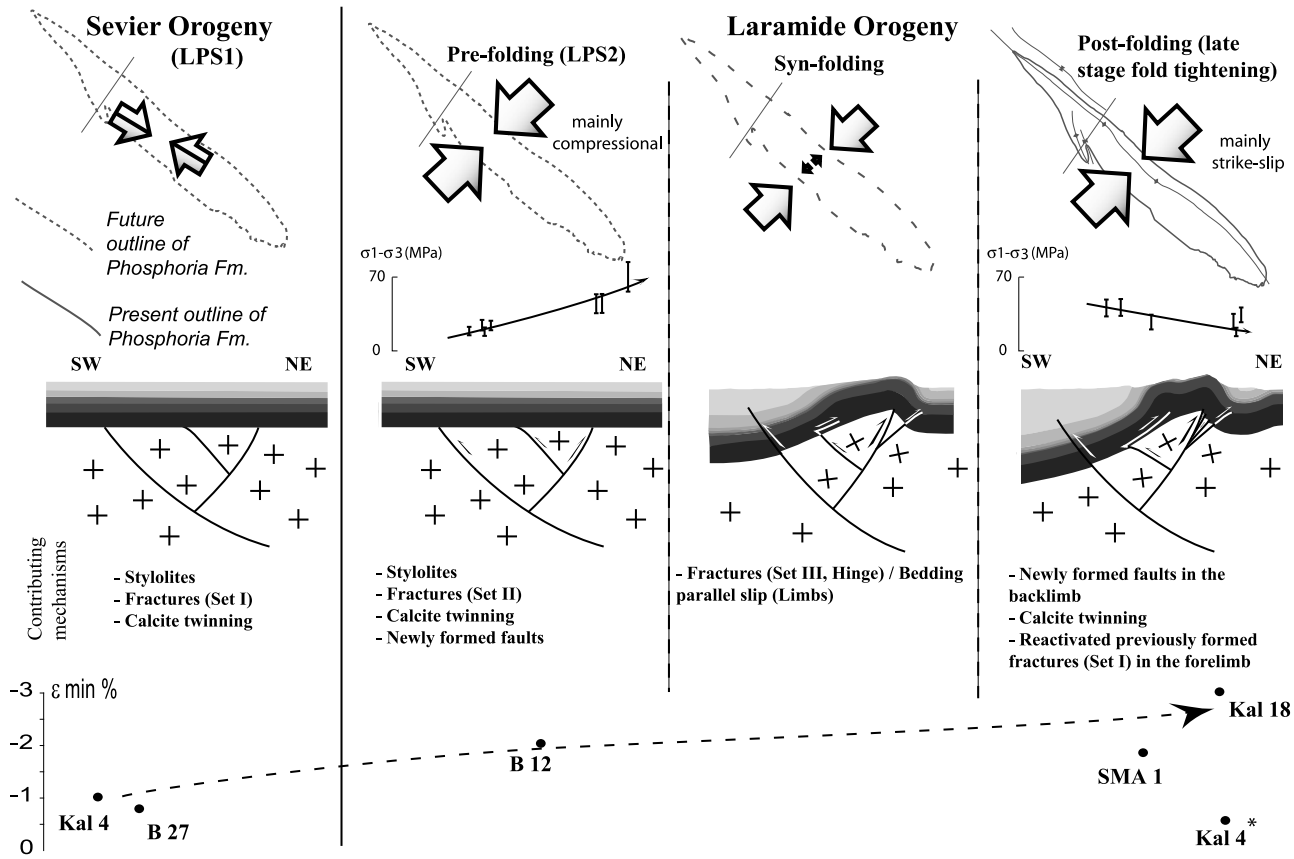

Figure 15. Sketch of different stages of fold evolution and related strain and differential stresses. For Kal 4*, the low calcite shortening related to the second strain tensor from sample Kal 4 likely reflects strain hardening during polyphase tectonic evolution.

implies a small decrease of σ_1. The increase of $(\sigma_1 - \sigma_h)$ together with σ_2/σ_3 permutation (σ_h switching from σ_2 to σ_3,) therefore implies a significant decrease of σ_h.

[87] In the forelimb $(\sigma_1 - \sigma_v)$ and $(\sigma_1 - \sigma_h)$ decrease. Because of the expected relaxation of the stress perturbation at fault tip during folding and even in the absence of significant synfolding erosion, σ_v likely slightly increases; it can be deduced that σ_1 decreases, and also σ_h (Figure 14). A striking point of this scenario is that the maximum differential stress increases in the backlimb from prefolding to postfolding stage. To account for this counterintuitive result, one can propose either significant hardening of the backlimb during folding or a decrease in pore fluid pressure during folding in response to fracturing of overlying impermeable formations such as the shaly Chugwater Formation by the development of the prefolding and synfolding fractures. Further work is needed to discuss these hypotheses.

5.5. Mechanisms of Deformation During Folding

[88] Mesoscale faulting, opening of vein sets and bedding-parallel slip observed in the field are associated with shear calcite fibers (and even gypsum fibers in local evaporite facies from Phosphoria Formation). In addition, stylolitization supports widespread pressure solution processes. We conclude that the rocks investigated (mainly) deformed within the elastic-frictional regime, with a noticeable amount of relaxation through plastic-viscous deformation. This is consistent with the mode of internal deformation of the limestones studied which occurred under a thin-twin regime, suggesting that temperature remained lower than 150°C–200°C [e.g., *Ferrill et al.*, 2004].

[89] Laramide small-scale faulting and twinning occurs mainly before folding as LPS, passively tilted later on as folding occurs, and after fold development (Figure 15).There are thus limited evidence of synfolding faulting and twinning; although this may be partly due to possible reorientation of stresses by bedding anisotropy during folding, which may mimic true prefolding structures, we suggest that internal strain is mainly achieved during the early and late stages of folding, probably during two peaks of stress which seem to predate immediately folding and to prevail after fold development (fold tightening stage [*Onasch*, 1983]). This is in agreement with the results of *Harris and van der Pluijm* [1998] that show that twinning fabrics in the Hudson valley fold-thrust belt fall into two populations: a strain population initiated as a prefolding LPS strain that was subsequently modified to its present orientation by active grain-scale rotation during flexural folding, and a second strain popu-

lation that reflects postfolding superimposed homogeneous strain, with no evidence of synfolding twinning strain.

[90] The way strain is accommodated "during" folding therefore deserves discussion. At the hinge where high curvature occurs, set III joints and veins that do strike parallel to the trend of the anticline accommodated bending stresses [*Bellahsen et al.*, 2006a; this study], while synfolding shortening oblique to bedding was mainly accommodated in the fold limbs by bedding-parallel slip. In the forelimb, bedding-parallel slip is clearly supported by slickenlines along bedding surfaces in the Madison Formation, tail cracks emanating from bedding surfaces in the Phosphoria Formation, and polished bedding surfaces of the Phosphoria Formation. In the backlimb, macroscopic evidence for bedding-parallel slip are much poorer, but the study of the anisotropy of magnetic susceptibility (which is beyond the scope of this paper) in the carbonates reveals there a magnetic foliation oblique to the bedding plane which is inconsistent with standard LPS fabrics but supports bed-parallel shearing (K. Amrouch et al., Constraints on deformation mechanisms during folding based on rock physical properties: Example of Sheep Mountain Anticline (Wyoming, USA), submitted to *Geophysical Journal International*, 2009). These observations are in agreement with the simulation results of *Sanz et al.* [2008] that greater bed-parallel slip occurs in the forelimb than in the hinge or the backlimb (Figure 15). In addition, even though set II joints and veins striking perpendicular to the fold axis mainly formed during LPS2 [*Bellahsen et al.*, 2006a; this study], it cannot be excluded that some also developed in the fold limbs during folding. Finally, the previously undescribed fractures postdating set II veins and interpreted as due to local extensional stresses, layer-parallel and in a plane close to vertical (section 4.1.3) may have also accommodated synfolding strain in the forelimb.

[91] Additional field observations of fracture surfaces and thin section analyses indicate that dip-slip or oblique-slip shearing has occurred along set I fractures in the forelimb at SMA within all studied formations: Madison, Tensleep, and Phosphoria [*Bellahsen et al.*, 2006a]. This study therefore supports the need of carefully considering prefolding joint and vein sets in realistic conceptual fold-fracture models as pointed out by *Bergbauer and Pollard* [2004], *Bellahsen et al.* [2006a], and *Ahmadhadi et al.* [2008], since reactivation of prefolding fracture sets may play an important role by preventing later development of "classical" fold-related fractures [*Guiton et al.*, 2003b; *Sassi et al.*, 2003].

[92] Our study provides a rather clear overview of the succession of various mechanisms active during the different stages of regional tectonic evolution and fold development (Figure 15). Laramide LPS2 was accommodated by stylolites, mesoscale reverse faulting and calcite twinning and was accompanied by mode I fracturing (set II) from the scale of the outcrop to the scale of the thin section. The stress field at that time was rather complex, at least in terms of magnitudes, because of stress perturbations caused by the underlying basement thrust fault. Synfolding strain was achieved through mode I fracturing (set III) and bedding-parallel slip mainly in the forelimb. Late stage fold tightening is marked by development of new mesoscale fault systems, calcite twinning and largely by shear reactivation of preexisting fracture sets.

[93] Our study interestingly supports that microstructures and macrostructures recorded at the same time the combination of far-field orogenic stresses and of the local sources of stress perturbation such as effect of the underlying basement fault, bedding rotation, bed-parallel slip and reactivation of early formed fractures. Despite some slight changes in stress orientations marked for instance by shear reactivation of earlier formed set II joints [e.g., *Fiore*, 2006] and stress permutations, these local effects have poorly influenced stress orientations during LPS and late stage fold tightening; in contrast, they greatly influence differential stress magnitudes.

6. Conclusion

[94] In this study, we have performed a combined analysis of various stress-strain indicators in order to unravel the distribution of stress in space and time prior to, during and just after folding above a high-angle thrust fault. Calcite twinning from both matrix and veins in various formations from Sheep Mountain Anticline recorded three tectonic stages: (1) a prefolding compression parallel to fold axis, likely related to pre-Laramide tectonism (Sevier orogeny LPS1 stage); this event appears to be of primary importance since fractures formed in this stress field were later reactivated during the fold-related stages, thus possibly preventing development of fold-related fractures, (2) a Laramide prefolding (LPS2) compression that trends perpendicular to the future fold axis; and (3) a Laramide fold-perpendicular compression postdating folding (late stage fold tightening). Prefolding and postfolding NE directed compressional stress and/or shortening were consistently recorded in matrix, prefolding veins and fold-related veins. These results are in good agreement with independent analyses of widespread joints and veins as well as striated microfaults measured throughout the fold. This demonstrates that stresses were consistently recorded from the scale of the grain/agreggate to the scale of the fold limb, thus allowing reliable extrapolation of local stress reconstructions (as, for instance, from oriented cores) to the whole fold structure and valuable description of the main lines of its stress-strain evolution.

[95] Calcite twin analysis additionally revealed significant variations of differential stress magnitudes across the fold, thus providing for the first time a complete picture of stress distribution in a fold. Our results point to an increase of LPS-related differential stress magnitudes from the backlimb to the forelimb possibly in relation with motion of the underlying basement fault, which did not propagate into the cover at that stage but likely induced stress concentrations above its upper tip. This result is confirmed by a simple numerical model.

[96] Beyond regional implications, this study highlights the potential of calcite twin analyses to yield a representative picture of successive regional/local stress and strain

patterns related to fold development, both in terms of orientations and magnitudes.

[97] **Acknowledgments.** The authors thank the two reviewers, E. Erslev and P. Laurent, for their constructive comments on the manuscript.

References

Ahmadhadi, F., J. M. Daniel, M. Azzizadeh, and O. Lacombe (2008), Evidence for pre-folding vein development in the Oligo-Miocene Asmari Formation in the Central Zagros Fold Belt, Iran, *Tectonics*, *27*, TC1016, doi:10.1029/2006TC001978.

Anderson, E. M. (1951), *The Dynamics of Faulting and Dyke Formation With Application to Britain*, 206 pp., Oliver and Boyd, London.

Angelier, J. (1990), Inversion of field data in fault tectonics to obtain the regional stress. III: A new rapid direct inversion method by analytical means, *Geophys. J. Int.*, *103*, 363–376, doi:10.1111/j.1365-246X.1990.tb01777.x.

Beaudoin, N. (2009), Étude géochimique et microstructurale de la fracturation de Sheep Mountain Anticline: Mise en évidence de paléocirculations de fluides et implications structurales, Master's thesis, 62 pp., Univ. Paris 6, Paris.

Bellahsen, N., P. Fiore, and D. D. Pollard (2006a), The role of fractures in the structural interpretation of Sheep Mountain Anticline, Wyoming, *J. Struct. Geol.*, *28*(5), 850–867, doi:10.1016/j.jsg.2006.01.013.

Bellahsen, N., P. Fiore, and D. D. Pollard (2006b), From spatial variation of fracture patterns to fold kinematics: A geomechanical approach, *Geophys. Res. Lett.*, *33*, L02301, doi:10.1029/2005GL024189.

Bergbauer, S., and D. D. Pollard (2004), A new conceptual fold-fracture model including prefolding joints, based on field data from the Immigrant Gap anticline, *Geol. Soc. Am. Bull.*, *116*, 294–307, doi:10.1130/B25225.1.

Bergerat, F., C. Bouroz-Weil, and J. Angelier (1992), Paleostresses inferred from macrofractures, Colorado Plateau, western U.S.A., *Tectonophysics*, *206*, 219–243, doi:10.1016/0040-1951(92)90378-J.

Bird, P. (1998), Kinematic history of the Laramide orogeny in latitudes 35°–49°N, western United States, *Tectonics*, *17*, 780–801, doi:10.1029/98TC02698.

Bird, P. (2002), Stress direction history of the western United States and Mexico since 85 Ma, *Tectonics*, *21*(3), 1014, doi:10.1029/2001TC001319.

Blackstone, D. L., Jr. (1990), Rocky Mountain foreland structure exemplified by the Owl Creek Mountains, Bridger Range and Casper Arch, central Wyoming, in *Wyoming Sedimentation and Tectonics, 41st Field Conference Guidebook*, edited by R. W. Specht, pp. 151–166, Wyo. Geol. Assoc., Casper.

Bourne, S. J. (2003), Contrast of elastic properties between rock layers as a mechanism for the initiation and orientation of tensile failure under remote compression, *J. Geophys. Res.*, *108*(B8), 2395, doi:10.1029/2001JB001725.

Brown, W. G. (1981), Surface and subsurface examples from the Wyoming foreland as evidences of a regional compressional origin of the Laramide orogeny, in *Rocky Mountain Foreland Basement Tectonics*, edited by D. W. Boyd and J. S. Lillegraven, *Contrib. Geol.*, *19*, 175–177.

Brown, W. G. (1988), Deformation style of Laramide uplifts in the Wyoming foreland, in *Interaction of the Rocky Mountain Foreland and the Cordilleran Thrust Belt*, edited by C.J Schmidt and W. J. Perry, Jr., *Mem. Geol. Soc. Am.*, *171*, 53–64.

Burkhard, M. (1993), Calcite twins, their geometry, appearance and significance as stress-strain markers and indicators of tectonic regime: A review, *J. Struct. Geol.*, *15*, 351–368, doi:10.1016/0191-8141(93)90132-T.

Callot, J. P., Y. Hamon, J. M. Mengus, and M. Barbier (2008), Sur la route de la Madison, Recherche de sites complémentaires à Sheep Mountain, Internal Rep. 60715, Inst. Fr. du Pét., Rueil-Malmaison, France.

Chapin, C. E., and S. M. Cather (1981), Eocene tectonics and sedimentation in the Colorado Plateau-Rocky Mountain area, in *Relations of Tectonics to Ore Deposits in the Southern Cordillera*, edited by W. R. Dickinson and W. D. Payne, *Ariz. Geol. Soc. Dig.*, *14*, 173–198.

Chapin, C. E., and S. M. Cather (1983), Eocene tectonics and sedimentation in the Colorado Plateau-Rocky Mountain area, in *Rocky Mountain Foreland Basin and Uplifts*, edited by J. D. Lowell, pp. 33–56, Rocky Mt. Assoc. of Geol., Denver, Colo.

Cooke, M. L., and C. A. Underwood (2001), Fracture termination and step-over at bedding interfaces due to frictional slip and interface opening, *J. Struct. Geol.*, *23*, 223–238, doi:10.1016/S0191-8141(00)00092-4.

Couples, G. D., and H. Lewis (2000), Effects of interlayer slip in model forced folds, in *Forced Folds and Fractures*, edited by J. W. Cosgrove and M. S. Ameen, *Geol. Soc. Spec. Publ.*, *169*, 129–144.

Craddock, J. P., and B. A. van der Pluijm (1999), Sevier-Laramide deformation of the continental interior from calcite twinning analysis, west-central North America, *Tectonophysics*, *305*, 275–286, doi:10.1016/S0040-1951(99)00008-6.

Dahlstrom, C. D. A. (1990), Geometric constraints derived from the law of conservation of volume and applied to evolutionary models for detachment folding, *Bull. Am. Assoc. Pet. Geol.*, *74*, 336–344.

De Sitter, L. V. (1956), *Structural Geology*, 551 pp., McGraw-Hill, New York.

Dickinson, W. R., and W. S. Snyder (1978), Plate tectonics of the Laramide orogeny, in *Laramide Folding Associated With Basement Block Faulting in the Western United States*, edited by V. Matthews, *Mem. Geol. Soc. Am.*, *151*, 355–366.

Dickinson, W. R., M. A. Klute, M. J. Hayes, S. U. Janecke, E. R. Lundin, M. A. Mckittrick, and M. D. Olivares (1988), Paleogeographic and paleotectonic setting of Laramide sedimentary basins in the central Rocky-Mountain region, *Geol. Soc. Am. Bull.*, *100*(7), 1023–1039, doi:10.1130/0016-7606(1988)100<1023:PAPSOL>2.3.CO;2.

Engebretson, D. C., A. Cox, and R. G. Gordon (1985), Relative motion between oceanic and continental plates in the Pacific basin, *Spec. Pap. Geol. Soc. Am.*, *206*.

Engelder, T. (1987), Joints and some fractures in rocks, in *Fracture Mechanics of Rock*, edited by B. Atkinson, pp. 27–69, Academic, New York.

Engelder, T., and D. C. P. Peacock (2001), Joint development normal to regional compression during flexural-flow folding: The Lilstock buttress anticline, Somerset, England, *J. Struct. Geol.*, *23*, 259–277, doi:10.1016/S0191-8141(00)00095-X.

Engelder, T., M. R. Gross, and P. Pinkerton (1997), Joint development in clastic rocks of the Elk Basin anticline, Montana-Wyoming, in *An Analysis of Fracture Spacing Versus Bed Thickness in a Basement-Involved Laramide Structure: 1997 Guidebook*, edited by T. Hoak, A. Klawitter, and P. Blomquist, pp. 1–18, Rocky Mt. Assoc. of Geol., Denver, Colo.

Erslev, E. A. (1993), Thrusts, back-thrusts and detachment of Rocky Mountain foreland arches, in *Laramide Basement Deformation in the Rocky Mountain Foreland of the Western United States*, edited by C. J. Schmidt, R. B. Chase, and E. A. Erslev, *Spec. Pap. Geol. Soc. Am.*, *280*, 339–358.

Etchecopar, A. (1984), Etude des états de contraintes en tectonique cassante et simulation de déformation plastique (approche mathématique), thèse doctorat-es-sciences, 270 pp., Univ. Sci. et Tech. du Languedoc, Montpellier, France.

Evans, M. A., and W. M. Dunne (1991), Strain factorization and partitioning in the North Mountain thrust sheet, central Appalachians, U.S.A., *J. Struct. Geol.*, *13*(1), 21–35, doi:10.1016/0191-8141(91)90098-4.

Evans, M. A., and R. D. Elmore (2006), Corrigendum to: Fluid control of localized mineral domains in limestone pressure solution structures, *J. Struct. Geol.*, *28*, 284–301, doi:10.1016/j.jsg.2005.10.004.

Evans, M. A., M. T. Lewchuk, and R. D. Elmore (2003), Strain partitioning of deformation mechanisms in limestones: Examining the relationship of strain and anisotropy of magnetic susceptibility (AMS), *J. Struct. Geol.*, *25*(9), 1525–1549, doi:10.1016/S0191-8141(02)00186-4.

Faill, R. T. (1973), Kink band folding. Valley and Ridge province, Pennsylvania, *Geol. Soc. Am. Bull.*, *84*, 1289–1314, doi:10.1130/0016-7606(1973)84<1289:KFVARP>2.0.CO;2.

Ferrill, D. A., A. P. Morris, M. A. Evans, M. Burkhard, R. H. Groshong, and C. M. Onasch (2004), Calcite twin morphology: A low temperature deformation geothermomenter, *J. Struct. Geol.*, *26*(8), 1521–1529, doi:10.1016/j.jsg.2003.11.028.

Fiore, P. E. (2006), 3D characterization and mechanics of brittle deformation in thrust fault related folds, Ph.D. thesis, Stanford Univ., Stanford, Calif.

Fischer, M. P., and M. S. Wilkerson (2000), Predicting the orientation of joints from fold shape: Results of pseudo-three-dimensional modeling and curvature analysis, *Geology*, *28*, 15–18, doi:10.1130/0091-7613(2000)28<15:PTOOJF>2.0.CO;2.

Forster, A., A. P. Irmen, and C. Vondra (1996), Structural interpretation of Sheep Mountain Anticline, Bighorn Basin, Wyoming, in *47th Field Conference Guidebook*, pp. 239–251, Wyo. Geol. Assoc., Casper.

Frizon de Lamotte, D., C. Souque, S. Grelaud, and P. Robion (2002), Early record of tectonic magnetic fabric during inversion of a sedimentary basin. Short review and examples from the Corbières transfer zone (France), *Bull. Soc. Geol. Fr.*, *173*, 461–469, doi:10.2113/173.5.461.

Graham, W. B. R. (2006), Influence of depositional setting and sedimentary fabric on mechanical layer evolution in carbonate aquifers, *Sediment. Geol.*, *184*, 203–224, doi:10.1016/j.sedgeo.2005.11.003.

Gries, R. (1983), North-south compression of Rocky Mountain foreland structures, in *Rocky Mountain Foreland Basin and Uplifts*, edited by J. D. Lowell, pp. 9–32, Rocky Mt. Assoc. of Geol., Denver, Colo.

Gries, R. (1990), Rocky Mountain foreland structures: Changes in compression direction through time, in *Petroleum and Tectonics in Mobile Belts*, edited by J. Letouzey, pp. 129–148, Technip, Paris.

Groshong, R. H., Jr. (1972), Strain calculated from twinning in calcite, *Geol. Soc. Am. Bull.*, *83*, 2025–2038, doi:10.1130/0016-7606(1972)83[2025:SCFTIC]2.0.CO;2.

Groshong, R. H., Jr. (1974), Experimental test of least-squares strain calculations using twinned calcite, *Geol. Soc. Am. Bull.*, *85*, 1855–1864, doi:10.1130/0016-7606(1974)85<1855:ETOLSG>2.0.CO;2.

Groshong, R. H., Jr., L. W. Teufel, and C. M. Gasteiger (1984), Precision and accuracy of the calcite strain-gauge technique, *Geol. Soc. Am. Bull.*, *95*, 357–363, doi:10.1130/0016-7606(1984)95<357:PAAOTC>2.0.CO;2.

Guiton, M., Y. L. Leroy, and W. Sassi (2003a), Activation of diffuse discontinuities and folding of the sedimentary layers, *J. Geophys. Res.*, *108*(B4), 2183, doi:10.1029/2002JB001770.

Guiton, M., W. Sassi, Y. L. Leroy, and B. D. M. Gauthier (2003b), Mechanical constraints on the chronology of fracture activation in the folded Devonian sandstone of the western Moroccan Anti-Atlas, *J. Struct. Geol.*, *25*, 1317–1330, doi:10.1016/S0191-8141(02)00155-4.

Harris, J. H., and B. A. van der Pluijm (1998), Relative timing of calcite twinning strain and fold-thrust belt development: Hudson Valley fold-thrust belt, New York, USA, *J. Struct. Geol.*, *20*, 21–31, doi:10.1016/S0191-8141(97)00093-X.

Hennier, J., and J. Spang (1983), Mechanisms for deformation of sedimentary strata at Sheep Mountain Anticline, Big Horn Basin, Wyoming, in *34th Annual Field Conference Guidebook*, pp. 97–111, Wyo. Geol. Assoc., Casper.

Hennings, P. H., J. E. Olson, and L. B. Thompson (2000), Combining outcrop data and three-dimensional structural models to characterize fractured reservoirs: An example from Wyoming, *AAPG Bull.*, *84*, 830–849.

Homberg, C., J. C. Hu, J. Angelier, F. Bergerat, and O. Lacombe (1997), Characterization of stress perturbations near major fault zones: Insights from field studies (Jura Mountains) and numerical modelling, *J. Struct. Geol.*, *19*(5), 703–718, doi:10.1016/S0191-8141(96)00104-6.

Hoppin, R. A. (1970), Structural development of Five Springs Creek area, Bighorn Mountains, Wyoming, *Geol. Soc. Am. Bull.*, *81*, 2403–2416, doi:10.1130/0016-7606(1970)81[2403:SDOFSC]2.0.CO;2.

Jamison, W. R., and J. H. Spang (1976), Use of calcite twin lamellae ton infer differential stress, *Geol. Soc. Am. Bull.*, *87*, 868–872, doi:10.1130/0016-7606(1976)87<868:UOCTLT>2.0.CO;2.

Johnson, K. M., and A. M. Johnson (2000), Localization of layer-parallel faults in San Rafael swell, Utah and other monoclinal folds, *J. Struct. Geol.*, *22*(10), 1455–1468, doi:10.1016/S0191-8141(00)00046-8.

Lacombe, O. (2001), Paleostress magnitudes associated with development of mountain belts: Insights from tectonic analyses of calcite twins in the Taiwan Foothills, *Tectonics*, *20*(6), 834–849, doi:10.1029/2001TC900019.

Lacombe, O. (2007), Comparison of paleostress magnitudes from calcite twins with contemporary stress magnitudes and frictional sliding criteria in the continental crust: Mechanical implications, *J. Struct. Geol.*, *29*, 86–99, doi:10.1016/j.jsg.2006.08.009.

Lacombe, O., and P. Laurent (1996), Determination of deviatoric stress tensors based on inversion of calcite twin data from experimentally deformed monophase samples: Preliminary results, *Tectonophysics*, *255*, 189–202, doi:10.1016/0040-1951(95)00136-0.

Lacombe, O., J. Angelier, P. Laurent, F. Bergerat, and C. Tourneret (1990), Joint analyses of calcite twins and fault slips as a key for deciphering polyphase tectonics: Burgundy as a case study, *Tectonophysics*, *182*, 279–300, doi:10.1016/0040-1951(90)90168-8.

Lacombe, O., J. Angelier, and P. Laurent (1993), Calcite twins as markers of recent compressional events in an active orogen: The reefal limestones of southern Taiwan as a case study, *C. R. Acad. Sci., Ser. II*, *316*, 1805–1813.

Lacombe, O., J. Angelier, M. Rocher, J. Bergues, H.-T. Chu, B. Deffontaines, and J.-C. Hu (1996a), Contraintes et plissement au front d'une chaîne de collision: L'exemple des calcaires récifaux pliocènes de Yutengping (Taiwan), *Bull. Soc. Geol. Fr.*, *167*, 361–374.

Lacombe, O., P. Laurent, and M. Rocher (1996b), Magnitude de la contrainte déviatorique pyrénéenne dans l'avant-pays nord-pyrénéen, *C. R. Acad. Sci., Ser. IIa*, *322*, 229–235.

Lacombe, O., K. Amrouch, F. Mouthereau, and L. Dissez (2007), Calcite twinning constraints on late Neogene stress patterns and deformation mechanisms in the active Zagros collision belt, *Geology*, *35*(3), 263–266, doi:10.1130/G23173A.1.

Ladd, R. E. (1979), The geology of Sheep Canyon Quadrangle, Wyoming, Ph.D. dissertation, 124 pp., Iowa State Univ., Ames.

Laurent, P. (1984), Les macles de la calcite en tectonique: Nouvelles méthodes dynamiques et premières applications, thèse doctorat-es-sciences, 324 pp., Univ. Sci. et Tech. du Languedoc, Montpellier, France.

Laurent, P., H. Kern, and O. Lacombe (2000), Determination of deviatoric stress tensors based on inversion of calcite twin data from experimentally deformed monophase samples. Part II. Axial and triaxial stress experiments, *Tectonophysics*, *327*, 131–148, doi:10.1016/S0040-1951(00)00165-7.

Letouzey, J. (1986), Cenozoic paleostress pattern in the Alpine foreland and structural interpretation in a platform basin, *Tectonophysics*, *132*, 215–231, doi:10.1016/0040-1951(86)90033-8.

Marfil, R., M. A. Caja, and M. Tsige (2005), Carbonate-cemented stylolites and fractures in the Upper Jurassic limestones of the Eastern Iberian Range, Spain: A record of palaeofluids composition and thermal history, *Sediment. Geol.*, *178*, 237–257, doi:10.1016/j.sedgeo.2005.05.010.

Marshak, S., K. Karlstrom, and J. M. Timmons (2000), Inversion of Proterozoic extensional faults: An explanation for the pattern of Laramide and Ancestral Rockies intracratonic deformation, United States, *Geology*, *28*, 735–738, doi:10.1130/0091-7613(2000)28<735:IOPEFA>2.0.CO;2.

McConaughy, D. T., and T. Engelder (2001), Joint initiation in bedded elastic rocks Source, *J. Struct. Geol.*, *23*(2–3), 203–221, doi:10.1016/S0191-8141(00)00091-2.

Neely, T. G., and E. A. Erslev (2009), The interplay of fold mechanisms and basement weaknesses at the transition between Laramide basement-involved arches, north-central Wyoming, U.S.A., *J. Struct. Geol.*, *31*(9), 1012–1027, doi:10.1016/j.jsg.2009.03.008.

Onasch, C. M. (1983), Dynamic analysis of rough cleavage in the Martinsburg formation, Maryland, *J. Struct. Geol.*, *5*(1), 73–81, doi:10.1016/0191-8141(83)90009-3.

Paylor, E. D., H. L. Muncy, H. R. Lang, J. E. Conel, and S. L. Adams (1989), Testing some models of foreland deformation at the Thermopolis anticline, southern Bighorn Basin, Wyoming, *Mt. Geol.*, *26*, 1–22.

Petit, J. P., and M. Barquins (1988), Can natural faults propagate under mode II conditions?, *Tectonics*, *7*(6), 1243–1256, doi:10.1029/TC007i006p01243.

Pollard, D. D., and A. Aydin (1988), Progress in understanding jointing over the past century, *Geol. Soc. Am. Bull.*, *100*, 1181–1204, doi:10.1130/0016-7606(1988)100<1181:PIUJOT>2.3.CO;2.

Price, N. J., and J. W. Cosgrove (1990), *Analysis of Geological Structures*, 511 pp., Cambridge Univ. Press, Cambridge, U. K.

Ramsay, J. G. (1974), Development of chevron folds, *Geol. Soc. Am. Bull.*, *85*, 1741–1754, doi:10.1130/0016-7606(1974)85<1741:DOCF>2.0.CO;2.

Reches, Z. (1978), Analysis of faulting in 3-dimensional strain field, *Tectonophysics*, *47*, 109–129, doi:10.1016/0040-1951(78)90154-3.

Rioux, R. L. (1994), Geologic map of the Sheep Mountain-Little Sheep Mountain area, Big Horn County, Wyoming, *U.S. Geol. Surv. Open File Rep., 94–191*.

Robion, P., S. Grelaud, and D. Frizon de Lamotte (2007), Pre-folding magnetic fabrics in fold-and-thrust belts: Why the apparent internal deformation of the sedimentary rocks from the Minervois basin (NE Pyrenees, France) is so high compared to the Potwar basin (SW Himalaya, Pakistan)?, *Sediment. Geol.*, *196*, 181–200, doi:10.1016/j.sedgeo.2006.08.007.

Rocher, M., O. Lacombe, J. Angelier, and H.-W. Chen (1996), Mechanical twin sets in calcite as markers of recent collisional events in a fold-and-thrust belt: Evidence from the reefal limestones of southwestern Taiwan, *Tectonics*, *15*, 984–996, doi:10.1029/96TC00625.

Rocher, M., O. Lacombe, J. Angelier, B. Deffontaines, and F. Verdier (2000), Cenozoic folding and faulting in the south Aquitaine Basin (France): Insights from combined structural and paleostress analyses, *J. Struct. Geol.*, *22*(5), 627–645, doi:10.1016/S0191-8141(99)00181-9.

Roure, F., and B. Colletta (1996), Cenozoic inversion structures in the foreland of the Pyrenees and Alps, in *Peri-tethys Memoir 2, Structure and Prospects of Alpine Basins and Forelands*, edited by P. A. Ziegler and F. Horvath, *Mém. Mus. Nat. Hist. Nat.*, *170*, 173–209.

Roure, F., D. G. Howell, S. Guellec, and P. Casero (1990), Shallow structures induced by deep-seated thrusting, in *Petroleum and Tectonics in Mobile Belts*, edited by J. Letouzey, pp. 15–30, Technip, Paris.

Rowe, K. J., and E. H. Rutter (1990), Paleostress estimation using calcite twinning - experimental calibration and application to nature, *J. Struct. Geol.*, *12*(1), 1–17, doi:10.1016/0191-8141(90)90044-Y.

Saint-Bezar, B., R. L. Hebert, C. Aubourg, P. Robion, R. Swenen, and D. Frizon de Lamotte (2002), Magnetic Fabric and petrographic investigations of hematite-bearing sandstones within ramp-related folds: Examples from the South Atlas Front (Morocco), *J. Struct. Geol.*, *24*, 1507–1520, doi:10.1016/S0191-8141(01)00140-7.

Sales, J. K. (1968), Crustal mechanics of Cordilleran foreland deformation, regional and scale-model approach, *Am. Assoc. Pet. Geol. Bull.*, *52*, 2016–2044.

Sans, M., J. Verges, E. Gomis, J. M. Parés, M. Schiattarella, A. Trave, F. Calvet, P. Santanach, and A. Doulcet (2003), Layer parallel shortening in salt-detached folds: Constraint on cross-section restoration, *Tectonophysics*, *372*, 85–104, doi:10.1016/S0040-1951(03)00233-6.

Sanz, P. F., R. I. Borja, and D. D. Pollard (2007), Mechanical aspects of thrust faulting driven by far-field compression and their implications to fold geometry, *Acta Geotech.*, *2*, 17–31, doi:10.1007/s11440-007-0025-0.

Sanz, P. F., D. D. Pollard, P. F. Allwardt, and R. I. Borja (2008), Mechanical models of fracture reactivation and slip on bedding surfaces during folding of the asymmetric anticline at Sheep Mountain, Wyoming, *J. Struct. Geol.*, *30*(9), 1177–1191, doi:10.1016/j.jsg.2008.06.002.

Sassi, W., M. L. E. Guiton, J. M. Daniel, J. L. Faure, J. M. Mengus, J. Schmitz, S. Delisle, Y. Leroy, and J. Masset (2003), Mechanical reconstruction of fracture development in Weber sandstone formation, Split Mountain (Utah), paper presented at American Association of Petroleum Geologist Meeting, Calgary, Alberta, Canada.

Savage, H. M., and M. L. Cooke (2004), The effect of non-parallel thrust fault interaction on fold patterns, *J. Struct. Geol.*, *26*, 905–917, doi:10.1016/j.jsg.2003.09.006.

Silliphant, L. J., T. Engelder, and M. R. Gross (2002), The state of stress in the limb of the Split Mountain anticline, Utah: Constraints placed by transected joints, *J. Struct. Geol.*, *24*(1), 155–172, doi:10.1016/S0191-8141(01)00055-4.

Sonnenfeld, M. D. (1996), An integrated sequence stratigraphic approach to reservoir characterization of the lower Mississippian Madison Limestone, emphasizing Elk Basin field, Bighorn basin, Wyoming and Montana, Ph.D. thesis, 438 pp., Colo. Sch. of Mines, Golden.

Stanton, H. I., and E. A. Erslev (2004), Sheep Mountain Anticline: Backlimb tightening and sequential deformation in the Bighorn Basin, Wyoming, in *53rd Wyoming Geological Association Guidebook*, pp. 75–87, Wyo. Geol. Assoc., Casper.

Stearns, D. W. (1968), Certain aspects of fractures in naturally deformed rocks, in *Rock Mechanics Seminar*, edited by R. E. Riecker, 97–118, Terr. Sci. Lab., Bedford, Mass.

Stearns, D. W., and M. Friedman (1972), *Reservoirs in Fractured Rocks*, *AAPG Mem.*1682–100.

Stone, D. S. (1969), Wrench faulting and Rocky Mountain tectonics, *Mt. Geol.*, *6*, 67–79.

Stone, D. S. (1993), Basement-involved thrust generated folds as seismically imaged in sub-surface of the central Rocky Mountain foreland, in *Laramide Basement Deformation in the Rocky Mountain Foreland of the Western United States*, edited by C. J. Schmidt, R. B. Chase, and E. A. Erslev, *Spec. Pap. Geol. Soc. Am.*, *280*, 271–318.

Stone, D. S. (2004), Rio thrusting, multi-stage migration and formation of vertically segregated Paleozoic oil pools at Torchlight Field on the Greybull Platform (eastern Bighorn basin): Implications for exploration, *Mt. Geol.*, *41*, 119–138.

Tavani, S., F. Storti, O. Fernandez, J. A. Munoz, and F. Salvini (2006), 3-D deformation pattern analysis and evolution of the Anisclo anticline, southern Pyrenees, *J. Struct. Geol.*, *28*, 695–712, doi:10.1016/j.jsg.2006.01.009.

Thomas, A. L. (1993), Poly3D: A three-dimensional, polygonal element, displacement discontinuity boundary element computer program with applications to fractures, faults, and cavities in the Earth's crust, M.S. thesis, Stanford Univ., Stanford, Calif.

Thomas, L. E. (1965), Sedimentation and structural development of the Bighorn Basin, *Am. Assoc. Pet. Geol. Bull.*, *49*, 1867–1877.

Turner, F. J., D. T. Griggs, and H. Heard (1954), Experimental deformation of calcite crystals, *Geol. Soc. Am. Bull.*, *65*, 883–934, doi:10.1130/0016-7606(1954)65[883:EDOCC]2.0.CO;2.

Twiss, R. J., and J. R. Unruh (1998), Analysis of fault slip inversions: Do they constrain stress or strain rate?, *J. Geophys. Res.*, *103*(B6), 12,205–12,222, doi:10.1029/98JB00612.

van der Pluijm, B. A., J. P. Craddock, B. R. Graham, and J. H. Harris (1997), Paleostress in cratonic north America: Implications for deformation of continental interiors, *Science*, *277*, 794–796, doi:10.1126/science.277.5327.794.

Varga, R. J. (1993), Rocky Mountain foreland uplifts: Products of rotating stress field or strain partitioning?, *Geology*, *21*, 1115–1118, doi:10.1130/0091-7613(1993)021<1115:RMFUPO>2.3.CO;2.

Wilkins, S. J. G., R. Michael, M. Wacker, Y. Eyal, and T. Engelder (2001), Faulted joints; kinematics, displacement-length scaling relations and criteria for their identification, *J. Struct. Geol.*, *23*, 315–327, doi:10.1016/S0191-8141(00)00098-5.

Wise, D. U., and C. M. Obi (1992), Laramide basement deformation in an evolving stress field, Bighorn Mountain front, Five Springs areas, Wyoming, *AAPG Bull.*, *76*, 1586–1600.

K. Amrouch, N. Bellahsen, and O. Lacombe, ISTEP, UMR 7193, Université Pierre et Marie Curie, CNRS, Aile 46-45 Etage 2, Boîte 129, 4, place Jussieu, F-75252 Paris CEDEX 05, France. (olivier.lacombe@upmc.fr)

J.-P. Callot and J.-M. Daniel, Division Géologie-Géochimie-Géophysique, Institut Français du Pétrole, 1-4 av. de Bois Préau, F-92852 Rueil-Malmaison CEDEX, France.